Mercury stable isotopes constrain atmospheric sources to the Ocean

Martin Jiskra[1,2,*,#], Lars-Eric Heimbürger-Boavida[2,3*,#], Marie-Maëlle Desgranges[3], Mariia V. Petrova[3], Aurélie Dufour[3], Beatriz Ferreira-Araujo[2], Jeremy Masbou[2], Jerome Chmeleff[2], Melilotus Thyssen[3], David Point[2], Jeroen E. Sonke[2,#]

[1]Environmental Geosciences, University of Basel, Switzerland

[2]Géosciences Environnement Toulouse, CNRS/IRD/Université Paul Sabatier Toulouse III, France.

[3]Aix Marseille Université, CNRS/INSU, Université de Toulon, IRD, Mediterranean Institute of Oceanography (MIO) UM 110, 13288, Marseille, France

*These authors contributed equally as 1st authors: M Jiskra, LE Heimbürger-Boavida

[#]Corresponding authors: martin.jiskra@unibas.ch, lars-eric.heimburger@mio.osupytheas.fr, jeroen.sonke@get.omp.eu

Keywords: GEOTRACES, marine mercury, Hg stable isotopes, Mediterranean Sea, Atlantic Ocean, atmospheric deposition, gas exchange, emission, invasion, biota, sediment

Human exposure to toxic mercury (Hg) is dominated by the consumption of seafood[1,2]. Earth system models suggest that Hg in marine ecosystems is supplied by atmospheric wet and dry Hg(II) deposition, with a 3 times smaller contribution from gaseous Hg(0) uptake[3,4]. Observations of marine Hg(II) deposition and Hg(0) gas exchange are sparse however[5], leaving the suggested importance of Hg(II) deposition[6] ill-constrained. Here we present the first Hg stable isotope measurements of total Hg (tHg) in surface and deep Atlantic and Mediterranean seawater and use it to quantify atmospheric Hg deposition pathways. We observe overall similar tHg isotope compositions, with median Δ^{200}Hg signatures of 0.02‰, lying in between atmospheric Hg(0) and Hg(II) deposition end-members. We use a Δ^{200}Hg isotope mass balance to estimate that seawater tHg can be explained by the mixing of 42% (24 to 50 %, median and interquartile range) atmospheric Hg(II) gross deposition and 58% (50 to 76 %) Hg(0) gross uptake. We measure and compile additional, global marine Hg isotope data including particulate Hg, sediments and biota and observe a latitudinal Δ^{200}Hg gradient indicating larger ocean Hg(0) uptake at high latitudes. Our findings suggest that global atmospheric Hg(0) uptake by the oceans is equal to Hg(II) deposition, which has implications for our understanding of atmospheric Hg dispersal and marine ecosystem recovery.

The consumption of seafood exposes humans to mono-methylmercury (MMHg), a toxin known to affect fetal and infant neurodevelopment and cardiovascular disease in adults[7]. MMHg is formed from inorganic mercury (Hg) in the ocean and biomagnifies along marine food webs to high levels[8–10]. Anthropogenic emission of Hg to the atmosphere outweighs natural emission five to ten-fold[11,12], and is thought to have more than tripled the Hg content of surface ocean waters[13]. Climate change and overfishing have been suggested to affect marine fish MMHg levels, and require detailed models of Hg cycling to assess future human exposure to Hg[14]. Earth system models of Hg biogeochemical cycling suggest that atmospheric Hg deposition to the modern open ocean is dominated by Hg(II) wet and dry deposition (4600 Mg y^{-1}, gross flux) compared to invasion, i.e. ocean uptake, of gaseous Hg(0) (1700 Mg y^{-1}, gross flux) in a 3:1 ratio[3,4] (Extended Data Figure 1). Rivers deliver similar amounts of Hg to coastal oceans (2050 to 5600 Mg y^{-1})[15–17] as atmospheric deposition, yet only 6% of river Hg is estimated to reach the open ocean[6]. Models also estimate that, of total deposited Hg(0) and Hg(II) forms, 4600 Mg y^{-1} (gross flux) is re-emitted to the atmosphere by (photo-)chemical and microbial reduction of Hg(II) to Hg(0) and evasion of Hg(0)[3,18]. The modern ocean is therefore a net sink of Hg (1700 Mg y^{-1}) with respect to the atmosphere (Extended Data Figure 1). Dissolved Hg(0) concentrations in surface waters are sporadically measured, and generally show Hg(0) supersaturation[19–21], supporting net Hg(0) evasion. The direction and magnitude of the large air-sea exchange of Hg(0) depends on the aqueous Hg(II) reduction and Hg(0) oxidation rates, and the wind driven air-sea Hg(0) exchange velocity in models[6]. The absence of direct, long-term Hg(0) flux measurements over the ocean and limited

observations of Hg(II) wet and dry deposition to oceans currently provide insufficient constraints for model validation of air-sea Hg(0) exchange, and Hg(II) deposition fluxes. This in turn hampers our capability to predict how Hg levels in the ocean will respond to curbed anthropogenic Hg emissions under the UN Minamata Convention on Mercury, and to climate change[12,22].

In terrestrial ecosystems, Hg stable isotopes have proven to be instrumental in understanding the relative importance of Hg(II) and Hg(0) deposition[23–25]. Atmospheric Hg(0) and Hg(II) in rainfall have different mass-dependent (MDF, δ^{202}Hg) and mass-independent isotope fractionation (MIF, Δ^{199}Hg and Δ^{200}Hg) signatures. Even-Hg MIF (Δ^{200}Hg) is thought to be generated exclusively by upper tropospheric and/or stratospheric photochemical reactions[26,27]. Δ^{200}Hg is therefore considered as a conservative tracer for atmospheric Hg deposition pathways[28]. So far, Hg stable isotopes in total unfiltered Hg (tHg) in seawater have only been measured in coastal seawater of the Canadian Arctic Archipelago, suggesting that 50% to 80% of tHg originated from coastal erosion and river input[29]. Analysis of particulate Hg (pHg) isotopes at the station ALOHA (22°N) near Hawaii suggested that atmospheric deposition of Hg(II) from rainfall was an important Hg source to the tropical Pacific surface ocean[30].

In this contribution we develop and apply a method for tHg isotope analysis of open ocean seawater, characterized by its (sub-)picomolar levels of tHg in all basins[31], to understand atmospheric supply of Hg to the ocean. We use the new Mediterranean and North-Atlantic tHg and pHg isotope observations together with published atmospheric Hg(II) and Hg(0) and marine pHg, sediment and biota Hg isotope data to show that ocean Hg(0) uptake is relatively more important than currently estimated.

Results and Discussion

Seawater Hg isotope composition

Oligotrophic Mediterranean station K2, 20 km off-shore (Extended Data Figure 2) showed tHg concentrations in June 2017, February and May 2019 (Figure 1a) that are slightly depleted in surface waters (0.80 pM), and peak at 300 m depth (1.1 pM), similar to previous observations[32,33]. Total methylated Hg (MeHg) concentrations peak at 400 - 600 m, (43 % of tHg), where oxygen levels reach their minimum due to microbial remineralization of particulate organic matter[33]. Surface tHg levels in the Bay of Marseille at Endoume pier were higher with 6.1 pM (4.9 to 6.7 pM, median and interquartile range (IQR), n = 8). In four samples from two Atlantic Ocean stations (St21, St38, Extended Data Figure 2), tHg increased with depth from 0.46 to 0.83 pM and represent the mixed layer (5 m, 20 m), intermediate water (650 m), and north-east Atlantic deep water (NEADW, 3345 m)[34]. MeHg in the two Atlantic profiles were similar to Mediterranean station K2 with low levels, 0.04 pM, at the surface and

elevated levels, 0.4 pM, at depth (54 % of tHg). pHg at the Mediterranean stations K1, K2 and Julio were low with a median of 0.10 pM (IQR: 0.08 to 0.15 pM, n = 16) for the 5 - 800 m depth range. Fram Strait pHg in Atlantic Ocean waters of the West-Spitzbergen current had higher pHg levels of 0.28 pM (0.23 to 0.31 pM, median and IQR, n = 9).

tHg isotope depth profiles for δ^{202}Hg, Δ^{199}Hg and Δ^{200}Hg signatures were replicated at station K2 during two sampling cruises in February and May 2019 and show reproducible results (Figure 1b-d). δ^{202}Hg is uniform with depth, with a median value of -0.09 ‰ (IQR: -0.31 to 0.00 ‰, n = 12). Overall, Δ^{199}Hg and Δ^{200}Hg are also near-zero, with median values of 0.06 and 0.01 ‰ respectively. The four North-Atlantic Ocean tHg samples show median δ^{202}Hg of -0.45 ‰, Δ^{199}Hg of 0.09‰, and Δ^{200}Hg of 0.06‰, and are therefore similar to Mediterranean waters. pHg isotope data for the Mediterranean Sea (n=19) and Atlantic (n=9) were broadly similar to tHg observations (Figures 1, 2, Supporting Information). Mediterranean sediments, had similar δ^{202}Hg = -0.75 ‰ (-0.76 to -0.74 ‰), Δ^{199}Hg = 0.05 ‰ (0.04 to 0.05 ‰) and Δ^{200}Hg = 0.03 ‰ (0.00 to 0.06 ‰) (median and (IQR), n = 4) to mean water column pHg, and were similar to sediment samples taken elsewhere in the Mediterranean Sea[35,36]. Overall, the tHg and pHg Δ^{199}Hg/Δ^{201}Hg slopes of 0.8 to 1.0 are indicative of photochemical MIF (Figure S2).

Atmospheric Hg(II) and Hg(0) deposition

We use Δ^{200}Hg to quantify the combined contribution of gross Hg(II) wet and dry deposition, and gross Hg(0) invasion to marine tHg and pHg (Methods, Eq. 3). It is important to clarify that Hg(0) gas exchange is bi-directional (Extended Data Figure 1), i.e. at any time atmospheric gaseous Hg(0) dissolves into the surface microlayer (invasion), and dissolved aqueous Hg(0) evades to the atmosphere. Although generally surface oceans are supersaturated in Hg(0), and gross Hg(0) evasion exceeds gross invasion, the gross Hg(0) invasion flux is substantial, around 1700 Mg y^{-1} in models, and an important contributor to marine Hg (Extended Data Figure 1). The Hg(II) dry and wet deposition flux is per definition a gross flux. Hg(II) deposition, after reduction to Hg(0) in ocean waters, does however contribute to the large Hg(0) emission flux. We exclude other marine Hg sources such as hydrothermal or river inputs. At Mediterranean station K2, this is justified by the absence of large rivers draining into the Ligurian Sea, and reflected in the open-ocean type tHg levels around 1 pM. The Rhône River reaches the Mediterranean, 100 km west of K2, at the continental shelf of the Gulf of Lions, and is carried further westward away from K2. Similarly, there is no hydrothermal activity within about 1000 km from the K2 station. At the Atlantic Ocean stations St21 and St38, no influence of river[37] or hydrothermal Hg inputs was found[34].

Modern, northern hemispheric Hg(II) wet deposition is characterized by a positive Δ^{200}Hg of 0.17 ‰ (0.11 ‰ to 0.22 ‰, median and (IQR), n = 106), for background sites with Hg concentrations < 25 ng L^{-1}; Extended Data Table 1). We also need to consider the Δ^{200}Hg of Hg(II) dry deposition, suggested to represent 40% of total atmospheric Hg(II) deposition to oceans[38]. Aerosol and fog water Hg(II) observations in the marine boundary layer (MBL) and free tropospheric gaseous Hg(II) in Atlantic air masses also have positive but slightly lower Δ^{200}Hg of 0.10 ‰ (0.07 to 0.1 ‰; median, IQR, n = 66)[39–41]. For end-member mixing calculations we estimated the Δ^{200}Hg of combined wet and dry Hg(II) deposition to vary between 0.13 and 0.15 ‰ with latitude (Extended Data Figure 6). Atmospheric Hg(0), the largest Hg pool in the atmosphere, exhibits negative Δ^{200}Hg of -0.05 ‰ (-0.08 to -0.03 ‰; median, IQR, n = 220, for continental background samples with Hg(0) concentrations < 2 ng m^{-3}; Extended Data Table 1). MBL Hg(0) observed at coastal sites and during cruises shows an identical Δ^{200}Hg of -0.06 ‰ (-0.08 ‰ to -0.02 ‰, median and IQR, n = 80, two-sided t.test, p = 0.96)[39,42,43].

Seawater tHg and pHg samples, including published Pacific Ocean pHg[30], show Δ^{200}Hg values statistically larger than atmospheric Hg(0) (one-sided t.test, p<0.001) and lower than Hg(II) end-members (one-sided t.test, p<0.001; Figure 2 & Figure 3A). Based on a Δ^{200}Hg mixing model (Methods, Eq. 3) we estimate the contribution of Hg(0) uptake, $f_{Hg(0)}$, to be 58 % (50 to 76 %, median and IQR, n = 16) to marine tHg and 58 % (39 to 82 %, n = 61) to pHg. This implies that the majority, i.e. approximately 58% of N-Atlantic and Mediterranean Sea tHg and pHg is derived from direct ocean Hg(0) uptake. We apply the same Δ^{200}Hg mass balance to the large body of published Hg isotope data in pelagic marine sediments and pelagic biota (n = 735, Extended Data Table 2). Similar to sea water tHg and pHg, global pelagic marine sediments and biota Δ^{200}Hg suggest a Hg(0) contribution, $f_{Hg(0)}$ of 57 % (49 to 65 %, n = 92) and 40 % (31 to 60 %, n= 643), respectively. The marine sediment and biota Δ^{200}Hg data cover a much larger geographical range than the tHg and pHg data, including the southern hemisphere, and indicate that, despite net Hg(0) evasion, gross ocean Hg(0) uptake is a globally important driver of marine pelagic ecosystem Hg levels.

Latitudinal Δ^{200}Hg variability

The validity of the Δ^{200}Hg mass balance hinges on two important details: 1. the link between aqueous Hg redox transformation rates and the gross or net nature of the Hg(II) deposition and Hg(0) uptake fluxes in the mass balance, and 2. latitudinal variation in marine Δ^{200}Hg observations. The current consensus in Hg cycling models is that marine aqueous Hg reduction and oxidation rates are fast[18,44,45], leading to global surface ocean oxidation and reduction fluxes of 2.6 x 10^6 Mg y^{-1} [45], which are 1000-fold larger than Hg deposition and air-sea exchange fluxes. This implies that the contrasting Δ^{200}Hg signatures of gross Hg(0) invasion (-0.05 ‰) and gross Hg(II) deposition (+0.14 ‰) will be rapidly

homogenized in the surface mixed layer before Hg(0) is partially re-emitted to the atmosphere. The Δ^{200}Hg derived Hg(0):Hg(II) deposition ratio therefore represents the gross deposition ratio. Secondly, our new seawater tHg and pHg Δ^{200}Hg observations are from 43° – 81°N, where Hg(II) wet deposition is known to be lower than in the northern hemispheric (sub-)tropics (Extended Data Figure 3). We therefore examined current best knowledge on the latitudinal variation of Hg(0) invasion vs Hg(II) deposition by a full latitudinal analysis of marine Δ^{200}Hg, combined wet and dry Hg(II) deposition flux, atmospheric and dissolved gaseous Hg(0) concentrations, and climatology (indicated by zonal 'reference model' in Figure 4). Gross Hg(II) deposition, gross Hg(0) invasion, gross Hg(0) evasion and net Hg(0) evasion, all based on a combination of published observations and models, (Figure 4, Extended Data Figure 5) vary as a function of latitude. Hg(0) invasion is primarily driven by observed atmospheric Hg(0) concentrations and wind speed, and is maximal at mid and high latitudes (Figure 4d). Hg(II) deposition is dominated by Hg(II) wet deposition in the sub-tropical northern hemisphere (Figure 4c). We use the Hg(II) deposition and Hg(0) invasion estimates (Figure 4, Extended Data Figure 5), together with Δ^{200}Hg end-members (Extended Data Figure 6, Extended Data Table 1) to predict the latitudinal marine Δ^{200}Hg distribution for the zonal 'reference model' (Figure 4a). Due to the asymmetric contributions of Hg(II) deposition and Hg(0) invasion to marine Hg, the predicted marine Δ^{200}Hg trend shows a maximum of 0.11 ‰ in the northern hemispheric (sub-)tropics and lower values of 0.02‰ at high latitudes. The observed marine Δ^{200}Hg distribution in water, sediments and biota is similar in shape but shifted to lower values compared to the predicted Δ^{200}Hg distribution, except between 45 – 65°N (Figure 4a). The Δ^{200}Hg observations therefore indicate a relatively larger Hg(0) invasion, or alternatively a smaller Hg(II) deposition contribution to pelagic marine Hg. By integrating the marine Δ^{200}Hg observations over latitude and weighting by sea surface area, we estimate a global ocean Hg(0) uptake contribution of 50% (IQR: 34% to 67%). Current best model estimates of global gross Hg(0) uptake and gross Hg(II) deposition at the ocean surface are 1700 Mg y^{-1} and 4600 Mg y^{-1} respectively.[3] Marine Hg isotope observations therefore suggest that gross Hg(0) uptake is equally important as gross Hg(II) deposition in a 1:1 ratio, compared to the Hg cycling model predicted ratio of 1:3. The latitudinal Δ^{200}Hg data are supported by the alternative even-Hg isotope signature Δ^{204}Hg, which mirrors Δ^{200}Hg (Extended Data Figure 7).

The marine Δ^{200}Hg composition suggests that our current understanding of the marine Hg budget is incomplete. We consider the most plausible reason for this to be that Hg(II) deposition to oceans is overestimated, either due to bias in coastal Hg(II) wet deposition observations (Figure 4c) by regional continental anthropogenic Hg emission sources, or due to overestimation of marine Hg(II) dry deposition for which no observations exist (Supporting Information text). Alternatively, current Hg(0) air-sea exchange parameterizations (Equations S1-3) could be incomplete, ignoring effects of the

surface micro-layer on the Hg(0) gas exchange velocity. In order to fit observed marine Δ^{200}Hg variability, a 2-3x lower marine Hg(II) deposition or 2-3x higher ocean Hg(0) uptake flux would be required (Figures 4c,d, Extended Data Figure 1; Supporting Information text). In either case, a larger relative contribution of Hg(0) to the oceans would have important impacts on the lifetime of anthropogenic Hg in atmosphere and surface ocean, and consequently on the anticipated recovery of ecosystems following aggressive Hg emission policy.

Acknowledgements

This work was supported by research grants ANR-17-CE34-0010 MERTOX to DP, FP7-IDEAS-ERC grant No 258537, and H2020 ERA-PLANET grant No 689443 via the iCUPE and iGOSP project to JES, Chantier Arctique Françaís funding via the Pollution in the Arctic System Project to JES and LEHB, H2020 Marie Sklodowska-Curie grant No 657195 and Swiss National Science Foundation grant PZ00P2_174101 to MJ, APOG DECOMAR, MISTRALS AT P&C and the AXA RF grants to LEHB, and the French National Research Agency (ANR-13-BS06-0014, ANR-12-PDOC-0025-01), the French National Centre for Scientific Research (CNRS-LEFE-CYBER), the LabexMER (ANR-10-LABX-19), and Ifremer. We are grateful to Géraldine Sarthou and Pascale Lherminier, chief scientists of the 2014 GEOVIDE cruise, and to Hélène Planquette for coordinating clean sampling. We thank Michiel Rutgers van der Loeff, Torsten Kanzow and the Alfred-Wegener-Institute for Polar and Marine Research for organizing the 2016 GRIFF cruise. We thank Emmanuel de Saint-Léger and Fabien Pérault of the technical division of INSU for support with operation at sea. We thank Laure Laffont for laboratory management, Olivier Grosso and Deny Malengros for technical assistance. We thank Luisa Metral from MARBEC and Frédéric Ménard from MIO for providing tuna fish samples from the Mediterranean Sea. We thank Joachim Kuss and Hannah Horowitz for discussion on gas exchange model parameterization. We thank the captains, crew and sampling teams onboard the RV Antedon II, RV Pourquoi Pas? and FS Polarstern for their support at sea. Thanks also go to the shipboard participants, captain and crew of the N/O l'Atalante for obtaining sediment samples from the 2015 VESPA cruise. VESPA was funded by the French Ministry of Research and Higher Education, with support from the governments of New Zealand and New Caledonia. We thank three anonymous reviewers for critical and constructive comments on our study.

Main text References

1. Sunderland, E. M. Mercury Exposure from Domestic and Imported Estuarine and Marine Fish in the U.S. Seafood Market. *Environmental Health Perspectives* **115**, (2007).

2. Lavoie, R. A., Bouffard, A., Maranger, R. & Amyot, M. Mercury transport and human exposure from global marine fisheries. *Scientific Reports* **8**, 6705 (2018).
3. Horowitz, H. M. *et al.* A new mechanism for atmospheric mercury redox chemistry: implications for the global mercury budget. *Atmospheric Chemistry and Physics* **17**, 6353–6371 (2017).
4. Travnikov, O. *et al.* Multi-model study of mercury dispersion in the atmosphere: atmospheric processes and model evaluation. *ATMOSPHERIC CHEMISTRY AND PHYSICS* **17**, 5271–5295 (2017).
5. Zhang, L., Zhou, P., Cao, S. & Zhao, Y. Atmospheric mercury deposition over the land surfaces and the associated uncertainties in observations and simulations: a critical review. *Atmospheric Chemistry and Physics* **19**, 15587–15608 (2019).
6. Zhang, Y. *et al.* A Coupled Global Atmosphere-Ocean Model for Air-Sea Exchange of Mercury: Insights into Wet Deposition and Atmospheric Redox Chemistry. *Environmental Science & Technology* **53**, 5052–5061 (2019).
7. Sheehan, M. C. *et al.* Global methylmercury exposure from seafood consumption and risk of developmental neurotoxicity: a systematic review. *Bulletin of the World Health Organization* **92**, 254–269 (2014).
8. Mason, R. P. & Fitzgerald, W. F. Alkylmercury species in the Equatorial Pacific. *Nature* **347**, 457–459 (1990).
9. Selin, N. E. Global Biogeochemical Cycling of Mercury: A Review. in *Annual Review of Environment and Resources* vol. 34 43–63 (2009).
10. Fitzgerald, W. F., Lamborg, C. H. & Hammerschmidt, C. R. Marine biogeochemical cycling of mercury. *Chemical Reviews* **107**, 641–662 (2007).
11. Li, C. *et al.* Unequal Anthropogenic Enrichment of Mercury in Earth's Northern and Southern Hemispheres. *ACS Earth Space Chem.* **4**, 2073–2081 (2020).
12. Outridge, P. M., Mason, R. P., Wang, F., Guerrero, S. & Heimbürger-Boavida, L. E. Updated Global and Oceanic Mercury Budgets for the United Nations Global Mercury Assessment 2018. *Environ. Sci. Technol.* **52**, 11466–11477 (2018).

13. Lamborg, C. H. *et al.* A global ocean inventory of anthropogenic mercury based on water column measurements. *Nature* **512**, (2014).
14. Schartup, A. T. *et al.* Climate change and overfishing increase neurotoxicant in marine predators. *Nature* **572**, 648–650 (2019).
15. Sunderland, E. M. & Mason, R. P. Human impacts on open ocean mercury concentrations. *Global Biogeochemical Cycles* **21**, GB4022 (2007).
16. Amos, H. M. *et al.* Global Biogeochemical Implications of Mercury Discharges from Rivers and Sediment Burial. *Environmental Science & Technology* **48**, 9514–9522 (2014).
17. Zhang, Y. *et al.* Biogeochemical drivers of the fate of riverine mercury discharged to the global and Arctic oceans. *Global Biogeochemical Cycles* **in review**, (2015).
18. Zhang, Y., Jaegle, L., Thompson, L. & Streets, D. G. Six centuries of changing oceanic mercury. *Global Biogeochemical Cycles* **28**, 1251–1261 (2014).
19. Soerensen, A. L. *et al.* Elemental Mercury Concentrations and Fluxes in the Tropical Atmosphere and Ocean. *Environmental Science & Technology* **48**, 11312–11319 (2014).
20. Kuss, J., Zülicke, C., Pohl, C. & Schneider, B. Atlantic mercury emission determined from continuous analysis of the elemental mercury sea-air concentration difference within transects between 50°N and 50°S. *Global Biogeochemical Cycles* **25**, (2011).
21. Wang, J., Xie, Z., Wang, F. & Kang, H. Gaseous elemental mercury in the marine boundary layer and air-sea flux in the Southern Ocean in austral summer. *Science of The Total Environment* **603–604**, 510–518 (2017).
22. Krabbenhoft, D. P. & Sunderland, E. M. Global change and mercury. *Science* **341**, 1457–1458 (2013).
23. Enrico, M. *et al.* Atmospheric mercury transfer to peat bogs dominated by gaseous elemental mercury dry deposition. *Environmental Science & Technology* (2016) doi:10.1021/acs.est.5b06058.

24. Demers, J. D., Blum, J. D. & Zak, D. R. Mercury isotopes in a forested ecosystem: Implications for air-surface exchange dynamics and the global mercury cycle. *Global Biogeochemical Cycles* **27**, 222–238 (2013).
25. Obrist, D. *et al.* Tundra uptake of atmospheric elemental mercury drives Arctic mercury pollution. *Nature* **547**, 201-+ (2017).
26. Chen, J., Hintelmann, H., Feng, X. & Dimock, B. Unusual fractionation of both odd and even mercury isotopes in precipitation from Peterborough, ON, Canada. *Geochimica et Cosmochimica Acta* **90**, 33–46 (2012).
27. Fu, X. W. *et al.* Mass independent fractionation of even and odd mercury isotopes during tropospheric mercury oxidation. *EarthArXiv* (2020) doi:https://eartharxiv.org/k5dwt/.
28. Enrico, M. *et al.* Holocene Atmospheric Mercury Levels Reconstructed from Peat Bog Mercury Stable Isotopes. *Environmental Science & Technology* **51**, 5899–5906 (2017).
29. Strok, M., Baya, P. A. & Hintelmann, H. The mercury isotope composition of Arctic coastal seawater. *Comptes Rendus Geoscience* **347**, 368–376 (2015).
30. Motta, L. C. *et al.* Mercury Cycling in the North Pacific Subtropical Gyre as Revealed by Mercury Stable Isotope Ratios. *Global Biogeochemical Cycles* **33**, 777–794 (2019).
31. Bowman, K. L., Lamborg, C. H. & Agather, A. M. A global perspective on mercury cycling in the ocean. *Science of The Total Environment* **710**, 136166 (2020).
32. Cossa, D., Averty, B. & Pirrone, N. The origin of methylmercury in open Mediterranean waters. *Limnology and Oceanography* **54**, 3 (2009).
33. Heimbürger, L.-E. *et al.* Methyl mercury distributions in relation to the presence of nanoand picophytoplankton in an oceanic water column (Ligurian Sea, North-western Mediterranean). *Geochimica et Cosmochimica Acta* **74**, 5549–5559 (2010).
34. Cossa, D. *et al.* Mercury distribution and transport in the North Atlantic Ocean along the GEOTRACES-GA01 transect. *BIOGEOSCIENCES* **15**, 2309–2323 (2018).

35. Gehrke, G. E., Blum, J. D. & Meyers, P. A. The geochemical behavior and isotopic composition of Hg in a mid-Pleistocene western Mediterranean sapropel. *Geochimica et Cosmochimca Acta* **73**, 1651–1665 (2009).
36. Ogrinc, N., Hintelmann, H., Kotnik, J., Horvatl, M. & Pirrone, N. Sources of mercury in deep-sea sediments of the Mediterranean Sea as revealed by mercury stable isotopes. *Scientific Reports* **9**, 11626 (2019).
37. Zhang, Y. *et al.* Biogeochemical drivers of the fate of riverine mercury discharged to the global and Arctic oceans. *Global Biogeochemical Cycles* **29**, 854–864 (2015).
38. Shah, V. & Jaeglé, L. Subtropical subsidence and surface deposition of oxidized mercury produced in the free troposphere. *Atmospheric Chemistry and Physics* **17**, 8999–9017 (2017).
39. Rolison, J. M., Landing, W. M., Cohen, M. D., Luke, W. & Salters, V. J. M. Isotopic composition of species-specific atmospheric Hg in a coastal environment. *Chemical Geology* **this issue**, (2012).
40. Washburn, S. J., Blum, J. D., Motta, L. C., Bergquist, B. A. & Weiss-Penzias, P. Isotopic Composition of Hg in Fogwaters of Coastal California. *Environ. Sci. Technol. Lett.* (2020) doi:10.1021/acs.estlett.0c00716.
41. Yu, B. *et al.* New evidence for atmospheric mercury transformations in the marine boundary layer from stable mercury isotopes. *Atmospheric Chemistry and Physics* **20**, 9713–9723 (2020).
42. Demers, J. D., Sherman, L. S., Blum, J. D., Marsik, F. J. & Dvonch, J. T. Coupling atmospheric mercury isotope ratios and meteorology to identify sources of mercury impacting a coastal urban-industrial region near Pensacola, Florida, USA. *Global Biogeochemical Cycles* **29**, 1689–1705 (2015).
43. Fu, X. *et al.* Isotopic Composition of Gaseous Elemental Mercury in the Marine Boundary Layer of East China Sea. *Journal of Geophysical Research: Atmospheres* **123**, 7656–7669 (2018).
44. Semeniuk, K. & Dastoor, A. Development of a global ocean mercury model with a methylation cycle: Outstanding issues. *Global Biogeochemical Cycles* **31**, 400–433 (2017).

45. Soerensen, A. L. *et al.* An Improved Global Model for Air-Sea Exchange of Mercury: High Concentrations over the North Atlantic. *Environmental Science & Technology* **44**, 8574–8580 (2010).

Author contributions

LEHB, JES, MJ and DP conceived the study. LEHB, MJ, DP, MP, MVP, MMD and JES performed sampling. JES, MJ, and LEHB developed and applied the tHg isotope pre-concentration methods. JES, MJ, JM and JC performed isotope measurements. MMD, MVP, AD, LEHB, MJ, JM, DP, and MT performed additional laboratory work. MJ, JES and LEHB analyzed the data. JES and MJ wrote the draft paper, which was improved by contributions from LEHB and DP, and commented by all authors.

Author Information The authors declare no competing financial interests.

Supplementary Information is available for this paper.

Data availability

Hg stable isotope and Hg speciation data that support the findings of this study are available from https://doi.org/10.5281/zenodo.4740464

Correspondence and requests for materials should be addressed to martin.jiskra@unibas.ch, lars-eric.heimburger@mio.osupytheas.fr, jeroen.sonke@get.omp.eu

Methods

The method for tHg in sea water consists of an ultra-clean shipboard sampling and post-cruise sample processing protocol using a standard stannous chloride ($SnCl_2$) reduction purge-and-trap method, based on the USEPA method 1631[46].

Sampling. Repeated, daily cruises were undertaken on the RV Antedon II from Marseille (France) to the nearby (20 km) oligotrophic, off-shore station K2 (42.98 N / 5.41 E / >1500 m depth) between 14/6/2017 and 21/6/2017, on 27/02/2019 and 22/05/2019. We used an epoxy-painted trace metal clean carousel, equipped with a conductivity-temperature-depth unit (CTD, Seabird SBE 911plus), and oxygen sensor (Seabird SBE 43), and 8x 10 L GOFLO trace metal clean bottles (General Oceanics). Samples were taken at up to 12 depths for Hg species, and at 4 depths for tHg and pHg isotopes, corresponding to surface waters (5 m), the chlorophyll-maximum (20 m), the oxygen minimum zone (400 m) and deep (800 m) waters. See SI for salinity, temperature, oxygen and fluorescence data.

Unfiltered seawater was drawn *via* acid-cleaned 6 mm FEP tubing into pre-cleaned 20 L Pyrex glass bottles with GL45 PFA Teflon caps. Bottles were filled to the 20 L mark, and not to the brim, in order to preserve a 3 L headspace for purge and trap purposes. Bottles were protected from sunlight and breaking risk in 70 L plastic barrels (Kruizinga.nl Ref#53-WHV70) by using polyurethane expansive foam to fit them in the barrels. We anticipate that future use of 20 L polycarbonate carboys are an alternative option, for safer sampling during rough seas. Unfiltered seawater was drawn from each GOFLO bottle into acid-cleaned and blank-tested 60 mL FEP Teflon bottles (Nalgene) for tHg and 250 mL PFA Teflon bottles (Savillex Purillex) for MeHg, MMHg and dissolved gaseous Hg (DGM = Hg^0 + dimethyl-Hg (DMHg)) analysis. All sampling was compliant with strict GEOTRACES trace metal clean sampling procedures[47]. Eight 20 L replicate samples of seawater from the Bay of Marseille were taken every three hours on 12/11/2019 at the Endoume pier. Seawater is continuously pumped at 20 L min^{-1} into the Mediterranean Institute of Oceanography (MIO) seawater sensing lab (SSL@MM). Samples were transported to MIO and processed within 24 h. Atlantic Ocean tHg samples were collected during the GEOVIDE cruise (GEOTRACES-GA01 transect), on board the RV "Pourquoi Pas?" between 15/05/2014 and 30/06/2014, similar to the MED Sea but using a 24 bottle trace metal clean carousel. tHg values for GEOVIDE have been published elsewhere[48].

Particulate Hg. pHg was sampled using in situ pumps (McLane LV08) at stations K1 (43.10 N, 5.49 E, 700 m depth, 10 km off-shore, continental slope), K2, and Julio (43.13 N, 05.36 E, 100 m-depth, 10 km off-shore, shelf) in the Mediterranean Sea on 16/06/2017, and at K2 on 22/05/2019; in Fram Strait Atlantic waters from 21/7/2016 to 1/9/2016 during the FS Polarstern PS100 GRIFF cruise (Geotraces-GN05 transect). Pre-burnt Millipore 142mm QMA, or GF/F were deployed for 1 - 3 h to collect particles from 148-792 L of seawater. Filter samples were frozen onboard, shipped frozen to MIO, freeze dried (Christ Gamma 1-16 LSCplus), and stored in the dark until analysis.

Pre-concentration of tHg from seawater for stable isotope analysis

The 20 L Mediterranean tHg samples were acidified and oxidized, within 12 h after sampling, at the MIO laboratory, using 5 mL 0.2 N BrCl (Sigma-Aldrich KBr and $KBrO_3$ salts) in concentrated bi-distilled 9 N HCl, leading to an initial sample HCl concentration of 0.0023 N. BrCl blanks were analyzed before addition, as it potentially constitutes the largest single component of the method blank. The volume of BrCl was optimized by visual inspection of the sample turning slightly yellow, indicating excess BrCl over reduced seawater components such as dissolved and particulate organic matter (DOC, POC, OM). Samples were let sit for 12 h, after which a 60 mL subsample was taken with an acid cleaned, 60 cm long, burette into pre-combusted 60 mL glass vials with acid-washed Teflon-lined caps for tHg

concentration analysis. This tHg subsample is compared to the shipboard 60mL tHg FEP sample and serves to verify that the 20 L bottles are neither contaminated, nor subjected to tHg loss.

tHg pre-concentration was started by replacing the GL45 PFA Teflon caps (Savillex) by GL45 two-port PFA Teflon caps (Savillex) to guide 60 cm long 6 mm OD (3 - 4 mm ID) Pyrex bubbling post with a 1 cm long P3 porosity frit (VitraPOR Micro Filter-Candle, Robuglas, Germany, custom assembled by Verres Vagner, Toulouse, France). The second port on the GL45 cap hosted a 10 cm long 6 mm OD FEP tube that was connected with a short piece of 10 mm OD, 4 mm ID silicone tubing to a shorter, 25 cm long, elbowed 6mm OD Pyrex bubbling post, with 1 cm long P2 frit (VitraPOR). The P2 bubbler post was then inserted into a 60 mL, 20 cm long glass test tube, filled with 6 mL of oxidizing 40 vol% inverse aqua regia (iAR) solution. The medium P2 bubbler frit inside the 40% iAR trap is critical to avoid over pressure and leaks of Hg(0) from the 20 L bottle. All glassware was pre-combusted at 530°C and Teflon-ware was cleaned by multiple bi-distilled HCl steps in a class 100 clean room.

Standard protocols for Hg(II) analysis by $SnCl_2$ reduction, such as EPA method 1631[46], use a large excess of $SnCl_2$ over Hg(II). While $SnCl_2$ does not pose a blank issue (purging it removes all Hg traces), it generates large volumes of toxic waste in each 20 L bottle after pre-concentration. We therefore tested up to 100x lower levels of anhydrous Sn(II)Cl_2 (Sigma-Aldrich). Hg(II) reduction by Sn(II) competes however with excess BrCl and natural oxygen present in seawater, i.e. Sn(II) is oxidized by BrCl and O_2 before it can reduce Hg(II). We therefore neutralized excess BrCl by adding 4 mL of NH_4.HCl (4.3 M) and verified disappearance of the yellow color. We then pre-purged (before adding $SnCl_2$) the 20 L sample with Hg-free argon at 300 mL min^{-1} for 3 h to remove > 90 % of dissolved oxygen. The 40% iAR solution trap was connected during pre-purging to trap any potential, though unlikely, loss of gaseous Hg from the sample. Adding $SnCl_2$ at this point, had however shown abundant precipitation of a fine white solid, presumably $SnCl_{2,s}$, which we remedied by adding an additional 80 mL volume of HCl to stabilize Sn(II) in the samples. Sn(II) addition was performed in two ways: i) 125 mL of $SnCl_2$ was slowly pumped with a peristaltic pump (Gilson) at 1.25 mL min^{-1}, and 1/16'' PFA tubing, *via* the central bubbling post into the bottle over 2 h; ii) the 125 mL was added instantly *via* the GL45 cap. No differences in Hg recovery were found between the two. Upon addition of $SnCl_2$ by pump or in batch, we purged the 20 L samples for 8 h at 300 mL min^{-1}, in order to quantitatively collect sample Hg into the oxidizing 40% iAR trap solution. At the end of 6 h of pre-concentration, the argon flow was stopped, and the 40 v% iAR traps removed and diluted with MQ water to 20 v% iAR and stored cold (4^{o}C) in the dark until analysis.

For the Atlantic Ocean tHg samples, a different pre-concentration technique was applied onboard which is described in detail in the Supporting Information. In brief, 48 L samples, stored in

Teflon (Tedlar) bags, were pumped at 5 mL min^{-1}, through an iodated activated carbon (IAC) cartridge onboard. The IAC sorbent was combusted back on land, at Geosciences Environnement Toulouse (GET), in a dual tube furnace set-up, and sample Hg(0) trapped in 6 mL 40% iAR. We abandoned this method due to higher blanks, challenging Hg recoveries from IAC, and slowness of sea water sample loading (1 week).

Procedural blanks and standards

Procedural Hg blanks, representing all laboratory manipulations, cleaning procedures, reagent additions, and different operators, were determined as follows. Following pre-concentration of a batch of 8 samples for tHg, the residual Hg-free seawater solution, was conserved in the 20 L bottle, and all reagents were newly added to 8 bottles as described above. The solutions were then purged, similar to samples, for 8 hours into newly prepared 6 mL 40% iAR traps. Eight procedural standards were pre-concentrated in a similar fashion: following blanks, once more all reagents were added to the remaining 20 L of Hg-free seawater solution, and 4 to 8 ng of NIST SRM 3133 Hg was added as internal standard to each bottle.

Particulate Hg concentration analysis

Total particulate Hg (pHg) concentrations were measured on 25 mm stamp-outs, by combustion – cold vapor atomic absorption spectrometry (CV-AAS, Leco AMA254) equipped with a low level optical cell at MIO. Certified reference material NRC MESS-3 marine sediment (91 ± 9 ng g^{-1}, 1σ) was used for quality control, with good results in the low, <1 ng Hg, range (88 ± 1 ng g^{-1}, 1σ). Remaining filter material was combusted whole on the dual tube furnace set-up at GET, following published protocols[49]. In brief, filters are rolled up, inserted in a 20 mm diameter, 15 cm long quartz tube, which is plugged from both sides with quartz wool. The sample tube is then inserted in a 140 cm long quartz tube, housed in two tube furnaces. The first furnace, hosting the sample tube, was heated from room temperature to 900°C over 6 h in an 80 mL min^{-1} flow of high purity oxygen. The released Hg(0) vapor and other volatile compounds passed through the 2nd pyrolizing oven, maintained at 1000°C continuously, and purged into a 40 vol% iAR oxidizing solution trap, that uses an elbowed, fritted, P2 porosity, Pyrex post. GF/F and GF/D filters melt at temperatures >530°C, but remain within the quartz sample tubes, blocked by the quartz wool. Final trapping solutions were diluted to 20%v iAR and stored cold in the dark until Hg concentration analysis by CV-AFS and Hg isotope analysis by MC-ICPMS. Reference material NIST SRM1632d coal was used for weekly quality control. Combustion purge and trapping recovery on samples, assessed by CV-AFS, was 104 ± 28%, 100 ± 28%, and 105 ± 21% (1σ) for the Mediterranean Sea, PS94 and PS100 cruise samples respectively.

tHg and Hg species concentration analysis

We added 40 µL of 0.2N BrCl to the 60 FEP Teflon bottles for ambient tHg analysis. Ambient tHg concentrations in 60 mL FEP Teflon bottle aliquots, in 20 L bottle aliquots before and after pre-concentration, and in 20% iAR solution traps were all analyzed in duplicate using a custom-made purge and trap system coupled to a cold vapor atomic fluorescence spectrometry (CV-AFS, Brooks Rand Model III), either at MIO, at GET, or shipboard[44]. The purge and trap system consists of 100 mL Teflon batch reactor (VWR), two electromagnetic valves (NResearch), a single gold trap (LECO), all connected by 1/8 inch FEP tubing to the CV-AFS (Brooks Rand Model 3). Seawater aliquots were 35 mL, and 20% iAR aliquots 100 µL. The CV-AFS was calibrated in the 1 - 20 pg range using NIST SRM 3133, and the NRC ORMS-5 certified reference material was always found within 10 % of the certified value (26 ± 1.3 ng L^{-1}, 1σ). MeHg, MMHg, and DGM were analyzed following our published protocols[50]. DMHg was calculated as the difference of MeHg and MMHg, and dissolved Hg(0) as the difference of DGM and DMHg. Details are given in the SI.

Hg isotope analysis

Hg stable isotope ratios of final 20 % iAR trap solutions were measured in duplicate during two sessions by cold vapor multi-collector inductively coupled plasma mass spectrometry (CV MC-ICPMS) at the Observatoire Midi-Pyrénées, Toulouse[51,52]. We used a CETAC ASX-520 autosampler and HGX-200 CV system coupled to a Thermo-Scientific Neptune PLUS, equipped with a 10^{12} Ω resistor, attributed to the ^{198}Hg isotope in order to improve isotope ratio precision in the 10-50 mV range. Samples and standard signals at 0.25 ng g^{-1} tHg levels were generally 180 mV on the ^{202}Hg isotope, at a sample introduction flow rate of 0.75 mL min^{-1}. Thallium was not used as an internal standard, and the 203 and 205 masses were monitored to survey Hg-hydride interferences (i.e. $^{202}Hg^{1}H$, and $^{202}Hg^{1}H^{1}H$), which were found to be negligible when using standard H-cones. ^{196}Hg and ^{204}Hg were not analyzed due to low abundance, and cup configuration limitations. MDF of Hg stable isotopes is reported in small delta notation (δ) in per mil (‰) deviation from to the reference NIST 3133 Hg standard:

$$\delta^{xxx}Hg = (({}^{xxx}Hg/{}^{198}Hg)_{sample}/({}^{xxx}Hg/{}^{198}Hg)_{NIST3133} - 1) \times 10^{3} \quad (1)$$

where 'xxx' refers to measured isotope masses: 199, 200, 201, and 202. Mass independent fractionation (MIF) is reported in capital delta notation[53], which is defined as the difference between the measured δ^{199}Hg, δ^{200}Hg, and δ^{201}Hg values and those predicted for MDF relative to δ^{202}Hg using the kinetic MDF law:

$$\Delta^{xxx}Hg = \delta^{xxx}Hg - SF^{xxx} \times \delta^{202}Hg \quad (2)$$

where SF^{xxx} is the mass-dependent scaling factor of 0.2520 for ^{199}Hg, 0.5024 for ^{200}Hg, and 0.7520 for ^{201}Hg. The long-term instrumental precision was assessed through repeated analysis of the UM-Almaden and ETH-Fluka Hg standard at 0.25 ng g^{-1} during the two analysis sessions. ETH-Fluka yielded values of −1.45 ± 0.20 ‰, 0.07 ± 0.11 ‰, 0.01 ± 0.14 ‰, 0.02 ± 0.09 ‰, 0.00 ± 0.18 ‰ (2σ, n = 10) for $\delta^{202}Hg$, $\Delta^{199}Hg$, $\Delta^{200}Hg$, and $\Delta^{201}Hg$ respectively, in agreement with published values[54]. UM-Almaden standard yielded -0.55 ± 0.16‰, -0.03 ± 0.11‰, -0.01 ± 0.03 ‰, -0.05 ± 0.23 ‰ (2σ, n = 10) respectively, in agreement with previously reported values[55].

pHg and tHg isotope method uncertainty

Mean pre-concentration recoveries for tHg isotope analysis were 90 ± 10% (1σ, n = 12) at Mediterranean station K2, 93 ± 18% (n=8) at Endoume coastal station, and 88 ± 31% (n = 4) for Atlantic Ocean samples. Procedural blanks were 0.23 ± 0.08 ng Hg (1σ, n = 4) for the $SnCl_2$ pre-concentration method, which is <10% of tHg in 20 L of seawater, e.g. typically 3 - 4 ng of tHg in this study. $SnCl_2$ method replication of eight 20L coastal Mediterranean samples (6 pM, analyzed at 1.6 ng g^{-1} by MC-ICPMS) shows good results with $\delta^{202}Hg$, $\Delta^{199}Hg$ and $\Delta^{200}Hg$ 2σ uncertainties of 0.23, 0.16, and 0.06 ‰. NIST SRM 3133 procedural standards returned $\delta^{202}Hg$, $\Delta^{199}Hg$, $\Delta^{200}Hg$, and $\Delta^{201}Hg$ values of 0.07 ± 0.23 ‰, -0.05 ± 0.16 ‰, 0.00 ± 0.06 ‰, -0.01 ± 0.18 ‰, 0.02 ± 0.21 ‰ and a mean recovery of 86 ± 16% (2σ, n = 8), suggesting no bias in the method.

pHg quality control results on NIST SRM 1632d yielded values of −1.75 ± 0.24 ‰, -0.04 ± 0.04 ‰, 0.00 ± 0.04 ‰, -0.02 ± 0.08 ‰ (2σ, n = 10) for $\delta^{202}Hg$, $\Delta^{199}Hg$, $\Delta^{200}Hg$ and $\Delta^{201}Hg$ respectively, in agreement with published values[49]. The 2σ uncertainty on pHg samples was taken to be the larger of either replicate sample analysis, procedural standard NIST SRM1632d, or secondary reference materials UM-Almaden or ETH-Fluka.

Most seawater pHg and tHg samples were analyzed in duplicate on different days. The final 2σ uncertainties reported for Mediterranean Sea and Atlantic Ocean pHg and tHg samples are the larger of the duplicate sample analysis, the 2σ on the eight NIST procedural standards (tHg), the 2σ on the ten NIST SRM 1632d standards, or the 2σ of the ETH Fluka or UM-Almaden standards.

Stable isotope data analysis

The fraction of Hg in marine samples derived from atmospheric Hg(0) ($f_{Hg(0)}$) was calculated using a binary isotope mixing model as follows:

$$\Delta^{200}Hg_{sample} = (1 - f_{Hg(0)}) \times \Delta^{200}Hg_{Hg(II)} + f_{Hg(0)} \times \Delta^{200}Hg_{Hg(0)} \quad (3)$$

503 where $\Delta^{200}Hg_{sample}$ represents the measured value of the marine sample (THg, pHg, sediment THg, biota
504 THg) or sample group. $\Delta^{200}Hg_{Hg(0)}$ and $\Delta^{200}Hg_{Hg(II)}$ end-member compositions are based on 392 published
505 data points (Extended Data Table 1). The $\Delta^{200}Hg_{Hg(II)}$ end-member composition varies as a function of
506 latitude, between values of 0.13 and 0.15 ‰ due to variable contributions of Hg(II) dry and wet
507 deposition (Extended Data Figure 6). The uncertainty on calculated $f_{Hg(0)}$ and $f_{Hg(II)}$ fractions was
508 estimated using a Monte Carlo error propagation approach, taking into account median and IQR in all
509 parameters (Extended Data Table 2).
510

511 **References**

512 46. USEPA. method 1631 Revision EMercury in Water by Oxidation, Purge and Trap, and Cold Vapor
513 Atomic Fluorescence Spectrometry, EPA-821/R-02/019, Washington, D.C., United States
514 Environmental Protection Agency, Office of Water (2002). (2002).
515 47. Cutter, G. J. *et al.* Sampling and Sample-handling Protocols for GEOTRACES Cruises. Version 3.0.
516 (2017).
517 48. Cossa, D. *et al.* Mercury distribution and transport in the North Atlantic Ocean along the
518 GEOTRACES-GA01 transect. *BIOGEOSCIENCES* **15**, 2309–2323 (2018).
519 49. Sun, R., Enrico, M., Heimbürger, L.-E., Scott, C. & Sonke, J. E. A double-stage tube furnace-acid-
520 trapping protocol for the pre-concentration of mercury from solid samples for isotopic analysis.
521 *Analytical and Bioanalytical Chemistry* **405**, 6771–6781 (2013).
522 50. Heimbürger, L. E. *et al.* Shallow methylmercury production in the marginal sea ice zone of the
523 central Arctic Ocean. *Scientific Reports* **doi:10.1038/srep10318**, (2015).
524 51. Jiskra, M., Sonke, J. E., Agnan, Y., Helmig, D. & Obrist, D. Insights from mercury stable isotopes on
525 terrestrial-atmosphere exchange of Hg(0) in the Arctic tundra. *Biogeosciences* **16**, 4051–4064
526 (2019).
527 52. Obrist, D. *et al.* Tundra uptake of atmospheric elemental mercury drives Arctic mercury
528 pollution. *Nature* **547**, 201-+ (2017).
529 53. Blum, J. D. & Bergquist, B. A. Reporting of variations in the natural isotopic composition of
530 mercury. *Analytical and Bioanalytical Chemistry* **388**, 353–359 (2007).
531 54. Jiskra, M. *et al.* Mercury Deposition and Re-emission Pathways in Boreal Forest Soils Investigated
532 with Hg Isotope Signatures. *Environmental Science & Technology* **49**, 7188–7196 (2015).
533 55. Bergquist, B. A. & Blum, J. D. Mass-Dependent and -Independent Fractionation of Hg Isotopes by
534 Photoreduction in Aquatic Systems. *Science* **318**, 417–420 (2007).
535 56. Shah, V. & Jaeglé, L. Subtropical subsidence and surface deposition of oxidized mercury
536 produced in the free troposphere. *Atmospheric Chemistry and Physics* **17**, 8999–9017 (2017).

57. Vermeesch, P. IsoplotR: A free and open toolbox for geochronology. *Geoscience Frontiers* **9**, 1479–1493 (2018).
58. Blum, J. D. & Johnson, M. W. Recent Developments in Mercury Stable Isotope Analysis. *Reviews in Mineralogy and Geochemistry* **82**, 733–757 (2017).
59. Gratz, L., Keeler, G., Blum, J. & Sherman, L. S. Isotopic composition and fractionation of mercury in Great Lakes precipitation and ambient air. *Environmental Science and Technology* **44**, 7764–7770 (2010).
60. Sherman, L. S., Blum, J. D., Keeler, G. J., Demers, J. D. & Dvonch, J. T. Investigation of Local Mercury Deposition from a Coal-Fired Power Plant Using Mercury Isotopes. *Environmental Science & Technology* **46**, 382–390 (2012).
61. Sherman, L. S. *et al.* Assessment of mercury exposure among small-scale gold miners using mercury stable isotopes. *Environmental Research* **137**, 226–234 (2015).
62. Wang, Z. *et al.* Mass-dependent and mass-independent fractionation of mercury isotopes in precipitation from Guiyang, SW China. *Comptes Rendus Geoscience* **347**, 358–367 (2015).
63. Donovan, P. M., Blum, J. D., Yee, D., Gehrke, G. E. & Singer, M. B. An isotopic record of mercury in San Francisco Bay sediment. *Chemical Geology* **349–350**, 87–98 (2013).
64. Sherman, L. S. *et al.* Mass-independent fractionation of mercury isotopes in Arctic snow driven by sunlight. *Nature Geoscience* **3**, 173–177 (2010).
65. Fu, X. W., Marusczak, N., Wang, X., Gheusi, F. & Sonke, J. E. The isotopic composition of total gaseous mercury in the free troposphere of the Pic du Midi Observatory (2877 m a.s.l, France). *Environmental Science & Technology* (2016) doi:10.1021/acs.est.6b00033.
66. Yu, B. *et al.* Isotopic Composition of Atmospheric Mercury in China: New Evidence for Sources and Transformation Processes in Air and in Vegetation. *Environmental Science & Technology* **50**, 9262–9269 (2016).

561 67. Ogrinc, N., Hintelmann, H., Kotnik, J., Horvatl, M. & Pirrone, N. Sources of mercury in deep-sea
562 sediments of the Mediterranean Sea as revealed by mercury stable isotopes. *Scientific Reports* **9**,
563 11626 (2019).
564 68. Gehrke, G. E., Blum, J. D. & Meyers, P. A. The geochemical behavior and isotopic composition of
565 Hg in a mid-Pleistocene western Mediterranean sapropel. *Geochimica et Cosmochimca Acta* **73**,
566 1651–1665 (2009).
567 69. Mil-Homens, M. *et al.* Tracing anthropogenic Hg and Pb input using stable Hg and Pb isotope
568 ratios in sediments of the central Portuguese Margin. *Chemical Geology* **this issue**, (2012).
569 70. Araujo, B. F., Hintelmann, H., Dimock, B., Almeida, M. G. & Rezende, C. E. Concentrations and
570 isotope ratios of mercury in sediments from shelf and continental slope at Campos Basin near
571 Rio de Janeiro, Brazil. *Chemosphere* **178**, 42–50 (2017).
572 71. Senn, D. B. *et al.* Stable Isotope (N, C, Hg) Study of Methylmercury Sources and Trophic Transfer
573 in the Northern Gulf of Mexico. *Environmental Science and Technology* **44**, 1630–1637 (2010).
574 72. Li, M. *et al.* Assessing Sources of Human Methylmercury Exposure Using Stable Mercury
575 Isotopes. *Environmental Science & Technology* **48**, 8800–8806 (2014).
576 73. Renedo, M. *et al.* Contrasting Spatial and Seasonal Trends of Methylmercury Exposure Pathways
577 of Arctic Seabirds: Combination of Large-Scale Tracking and Stable Isotopic Approaches. *Environ.*
578 *Sci. Technol.* **54**, 13619–13629 (2020).
579 74. Motta, L. C., Blum, J. D., Popp, B. N., Drazen, J. C. & Close, H. G. Mercury stable isotopes in flying
580 fish as a monitor of photochemical degradation of methylmercury in the Atlantic and Pacific
581 Oceans. *Marine Chemistry* **223**, 103790 (2020).
582 75. Madigan, D. J. *et al.* Mercury Stable Isotopes Reveal Influence of Foraging Depth on Mercury
583 Concentrations and Growth in Pacific Bluefin Tuna. *Environ. Sci. Technol.* **52**, 6256–6264 (2018).
584 76. Blum, J. D., Popp, B. N., Drazen, J. C., Choy, C. N. & Johnson, M. W. Methylmercury production
585 below the mixed layer in the North Pacific Ocean. *Nature Geoscience* **DOI: 10.1038/NGEO1918**,
586 (2013).

77. Blum, J. D. *et al.* Mercury isotopes identify near-surface marine mercury in deep-sea trench biota. *Proceedings of the National Academy of Sciences* **117**, 29292–29298 (2020).
78. Sun, R. *et al.* Methylmercury produced in upper oceans accumulates in deep Mariana Trench fauna. *Nature Communications* **11**, 3389 (2020).
79. Point, D. *et al.* Methylmercury photodegradation influenced by sea ice cover in Arctic marine ecosystems. *Nature Geoscience* **4**, 188–194 (2011).
80. Day, R. D. *et al.* Mercury Stable Isotopes in Seabird Eggs Reflect a Gradient from Terrestrial Geogenic to Oceanic Mercury Reservoirs. *Environ. Sci. Technol.* **46**, 5327–5335 (2012).
81. Le Croizier, G. *et al.* Mercury isotopes as tracers of ecology and metabolism in two sympatric shark species. *Environmental Pollution* **265**, 114931 (2020).
82. Le Croizier, G. *et al.* The Twilight Zone as a Major Foraging Habitat and Mercury Source for the Great White Shark. *Environ. Sci. Technol.* (2020) doi:10.1021/acs.est.0c05621.
83. Renedo, M., Amouroux, D., Pedrero, Z., Bustamante, P. & Cherel, Y. Identification of sources and bioaccumulation pathways of MeHg in subantarctic penguins: a stable isotopic investigation. *Scientific Reports* **8**, 8865 (2018).
84. Renedo, M. *et al.* A “seabird-eye” on mercury stable isotopes and cycling in the Southern Ocean. *Science of The Total Environment* **742**, 140499 (2020).

611 **Figures**

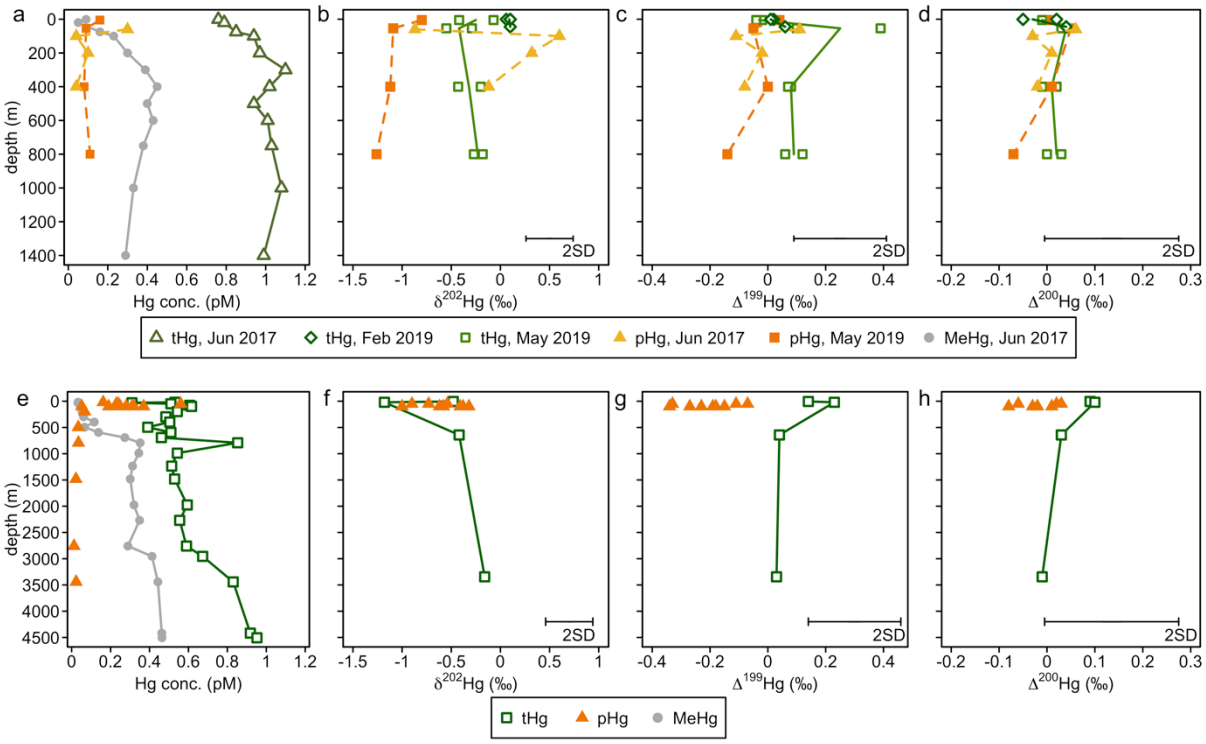

612

613

614 Figure 1a-h. Depth profiles of seawater Hg species concentrations and total and particulate Hg stable
615 isotope composition at station K2 in the Mediterranean Sea (a-d) and the North Atlantic (e-h). a) and
616 e): tHg, pHg, and MeHg concentrations in pmol L^{-1} (conc. pM). b) and f): mass-dependent fractionation
617 (δ^{202}Hg), c) and g): odd mass-independent fractionation (Δ^{199}Hg), d) and h): even mass-independent
618 fractionation (Δ^{200}Hg). Open symbols represent values for tHg and filled symbols pHg. The lines
619 represent averages of replicate analysis of the same sample. Two standard deviation (2SD)
620 uncertainties on Hg concentrations are 10%. The North Atlantic profile is a composite profile from two
621 stations at 47° and 59°N, and the Fram Strait at 79° to 81°N.

622

623

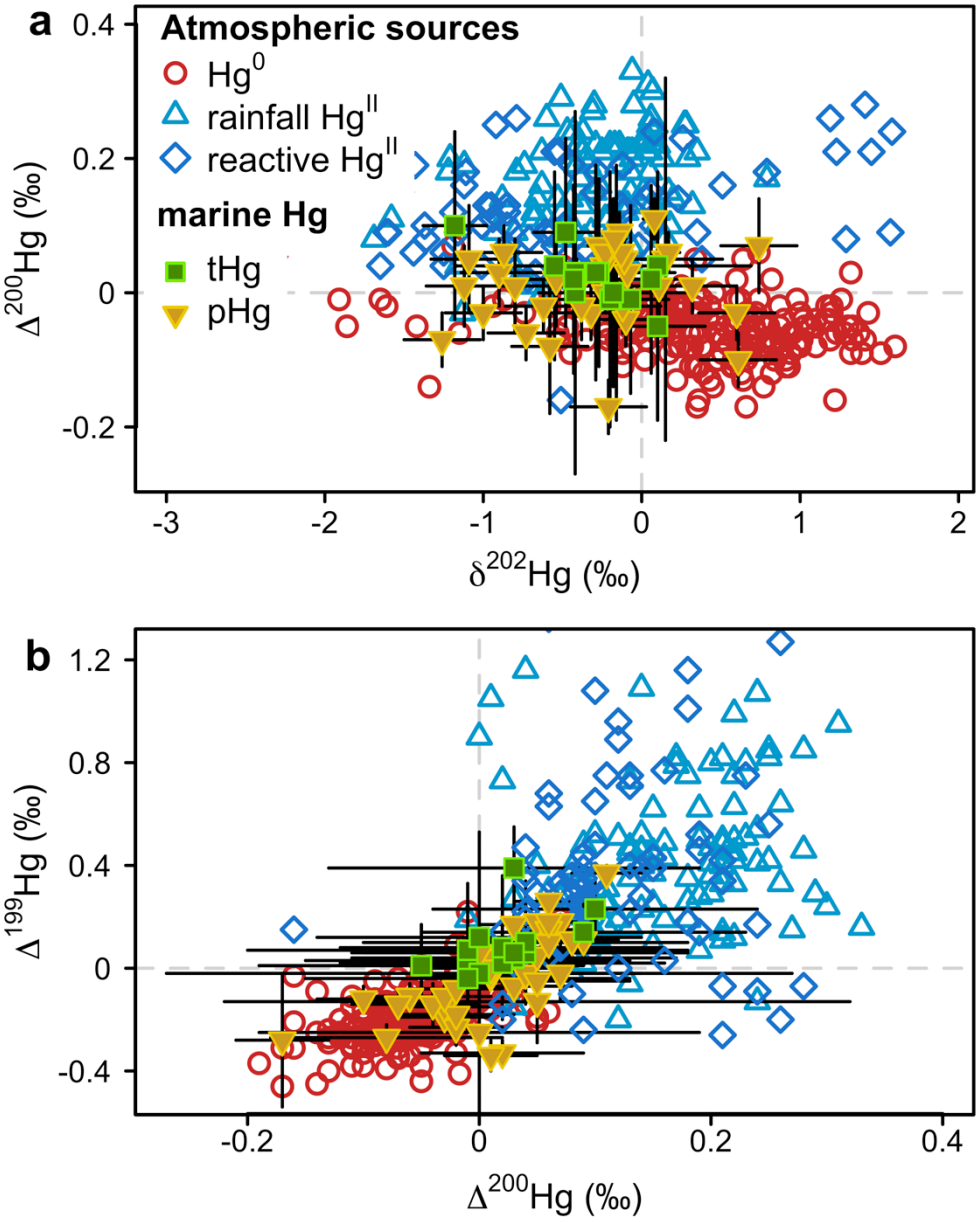

Figure 2. Hg stable isotope composition of atmospheric Hg deposition sources (gaseous Hg(0) and Hg(II) in rainfall), and seawater (total (tHg) and particulate (pHg)). a) even-isotope mass independent fractionation (Δ^{200}Hg) vs. mass dependent fractionation (δ^{202}Hg), and b) odd-isotope mass independent fractionation (Δ^{200}Hg) vs. even-isotope mass independent fractionation (Δ^{200}Hg). Values of atmospheric sources are from the literature (see Extended Data Table 1), tHg values are from this study, pHg from this study and ref.[30]. Error bars represent the two standard deviation (2SD) uncertainties of individual samples.

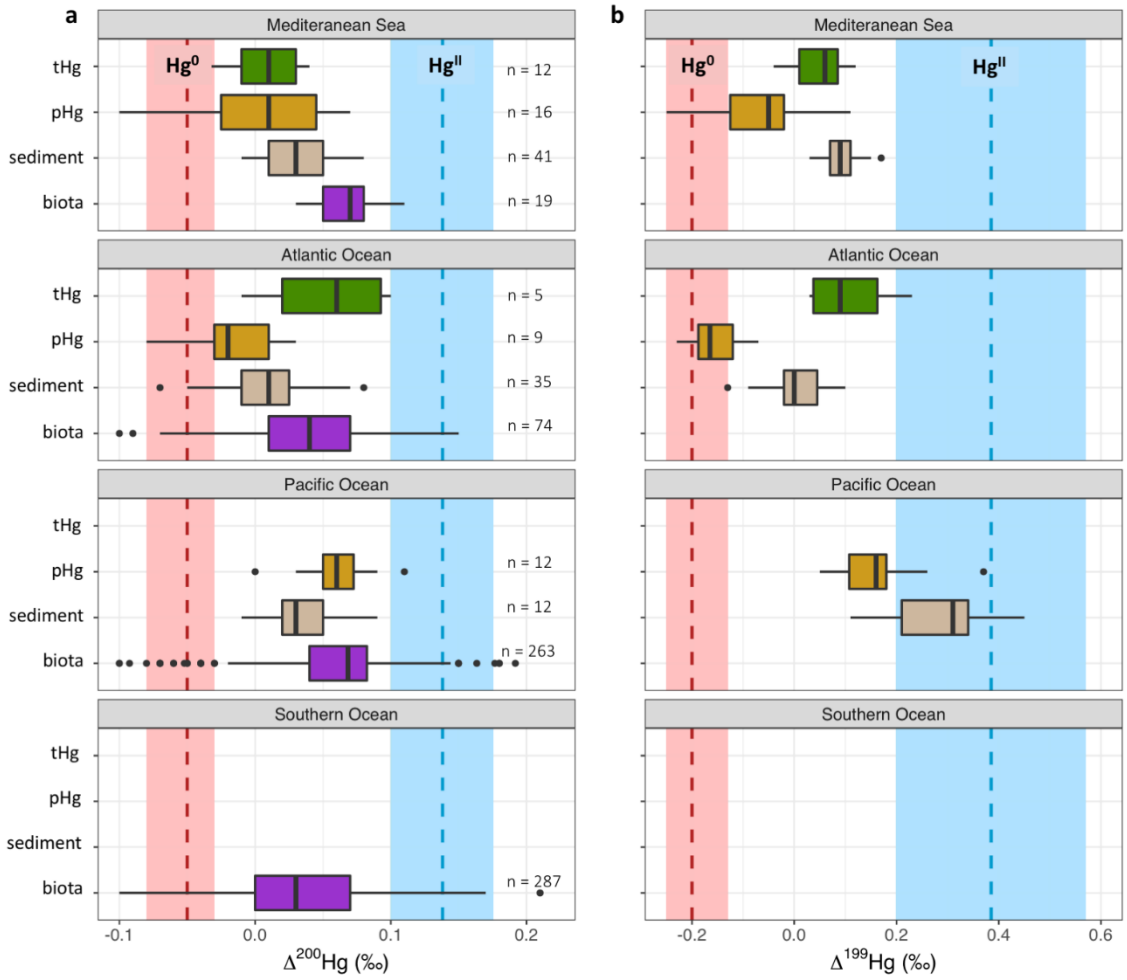

Figure 3. Hg stable isotope composition in different ocean basins for total Hg (tHg) and particulate Hg (pHg) in seawater, marine sediments and marine fish. a) Even-isotope mass-independent signature (Δ^{200}Hg) and b) Odd-isotope mass-independent signature (Δ^{199}Hg). tHg values are from this study, pHg from this study and from ref.[30], data for sediments and biota are from literature (Extended Data Table 1). The atmospheric deposition sources are shown as vertical bars in red for Hg(0) and blue for reactive and rainfall Hg(II) , the dashed line represents the mean and the shaded area the interquartile range (IQR). Marine samples are shown as horizontal boxes, where the bold line represents the median, the boxes the IQR, the whiskers 1.5 times the IQR and outliers are represented by dots. For biota, Δ^{199}Hg are not shown in this Figure as these values are heavily affected by MMHg photo-demethylation.

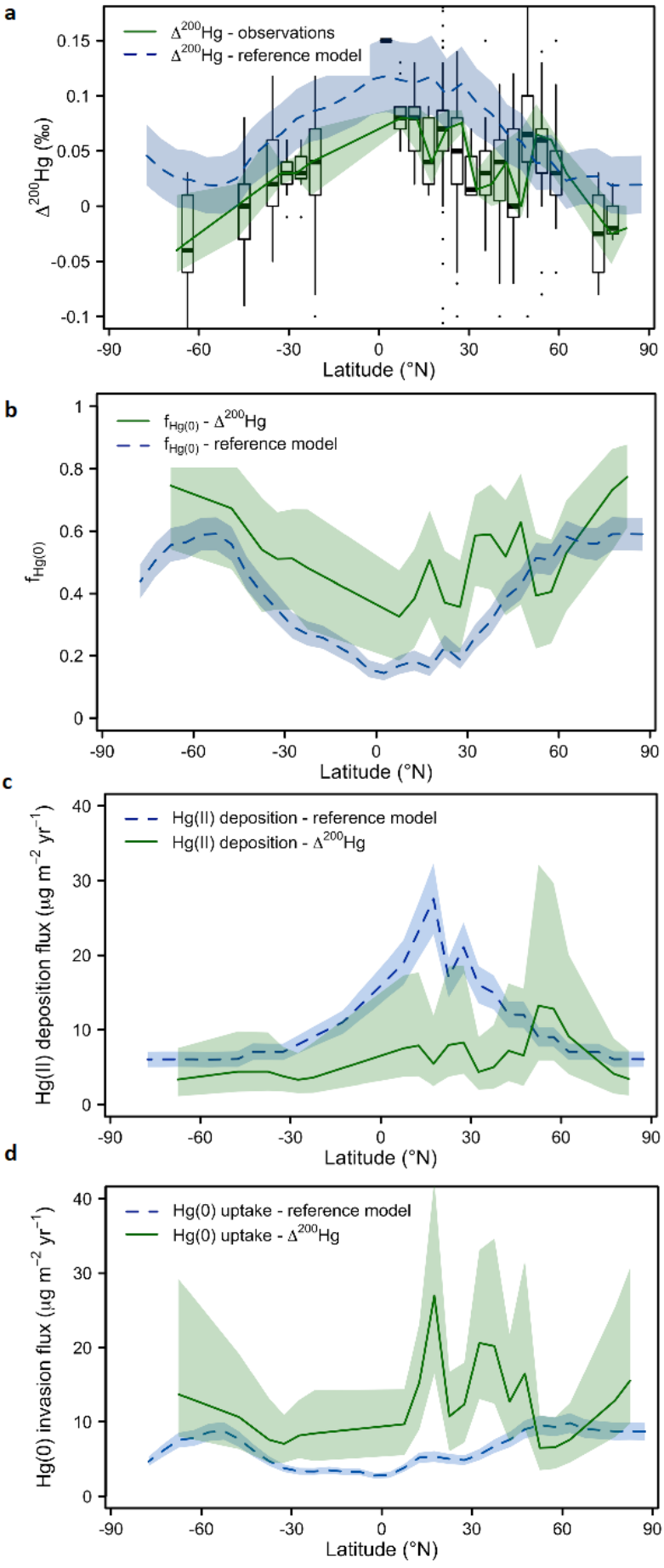
a
Δ200Hg - observations
Δ200Hg - reference model
Δ200Hg (‰)
Latitude (°N)
b
fHg(0) - Δ200Hg
fHg(0) - reference model
fHg(0)
Latitude (°N)
c
Hg(II) deposition - reference model
Hg(II) deposition - Δ200Hg
Hg(II) deposition flux (μg m−2 yr−1)
Latitude (°N)
d
Hg(0) uptake - reference model
Hg(0) uptake - Δ200Hg
Hg(0) invasion flux (μg m−2 yr−1)
Latitude (°N)

645

Figure 4: Latitudinal variation in atmospheric Hg sources and deposition fluxes to the global Ocean. Zonal 'Reference model' refers to the combination of zonal model and observation derived fluxes; i.e. the gas-exchange model which assimilates atmospheric and dissolved Hg(0) observations, 3D model global Hg(II) dry deposition[3], and Hg(II) wet deposition observations (see SI text, Extended Data Figures 3-6). a) Box plot for observed and reference model predicted marine Δ^{200}Hg in 5° latitude bins. The bold horizontal line represents the median, the boxes the interquartile range (IQR), the whiskers 1.5 times the IQR and dots are outliers. b) The Δ^{200}Hg-derived and reference model derived fraction of ocean Hg(0) uptake relative to total atmospheric Hg deposition. c) The Δ^{200}Hg-derived and reference model Hg(II) deposition fluxes. d) The Δ^{200}Hg-derived and reference model ocean Hg(0) uptake flux. All fluxes in μg m^{-2} y^{-1}. All lines represent medians and the shaded areas IQR. The green Δ^{200}Hg-based curves in panels c) and d) represent the gross Hg(II) deposition and gross Hg(0) invasion needed to reconcile marine Δ^{200}Hg observations in panel a), i.e. either lower Hg(II) deposition, or higher ocean Hg(0) uptake (see Supporting Information text).

660 **Extended Data Items**

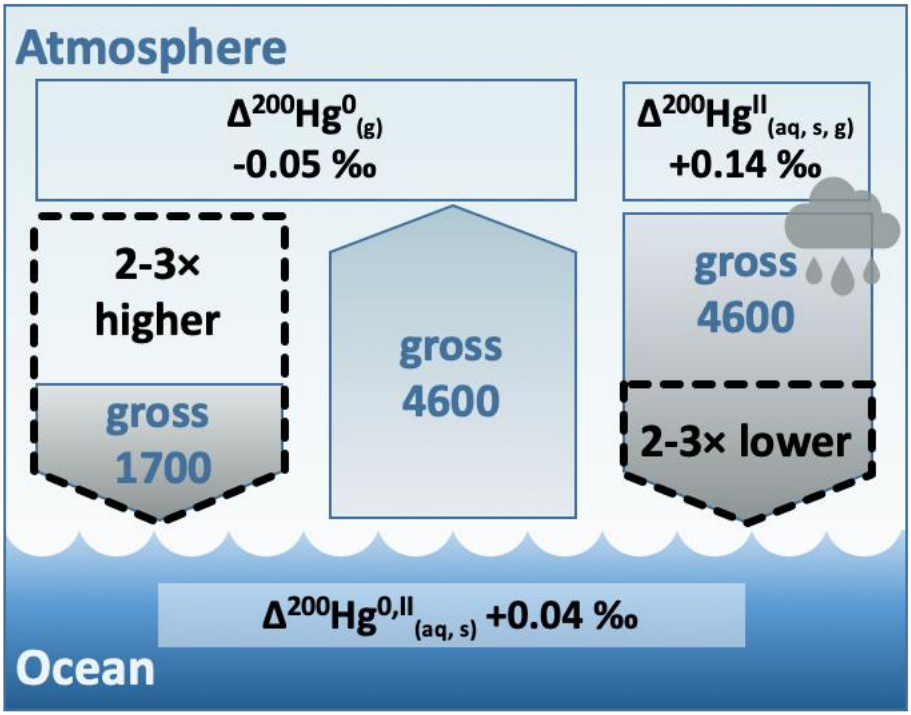

661

662 **Extended Data Figure 1. Summary of marine Hg(II) deposition and Hg(0) air-sea exchange fluxes.**
663 Gross fluxes (solid arrows, Mg y^{-1}) are based on published model estimates[3]. Hg(0) exchange is bi-
664 directional, meaning that despite surface ocean Hg(0) supersaturation and large Hg(0) evasion, Hg(0)
665 invasion is substantial. Marine Δ^{200}Hg signatures of 0.04‰ indicate a relatively more important
666 contribution of the atmospheric Hg(0) end-member to marine Hg than current 3D models suggest. This
667 indicates that either 3D model Hg(II) deposition is overestimated or that Hg(0) invasion is
668 underestimated (black dotted arrows, indicating 2-3x lower or 2-3x higher fluxes, required to fit Δ^{200}Hg
669 data).

670

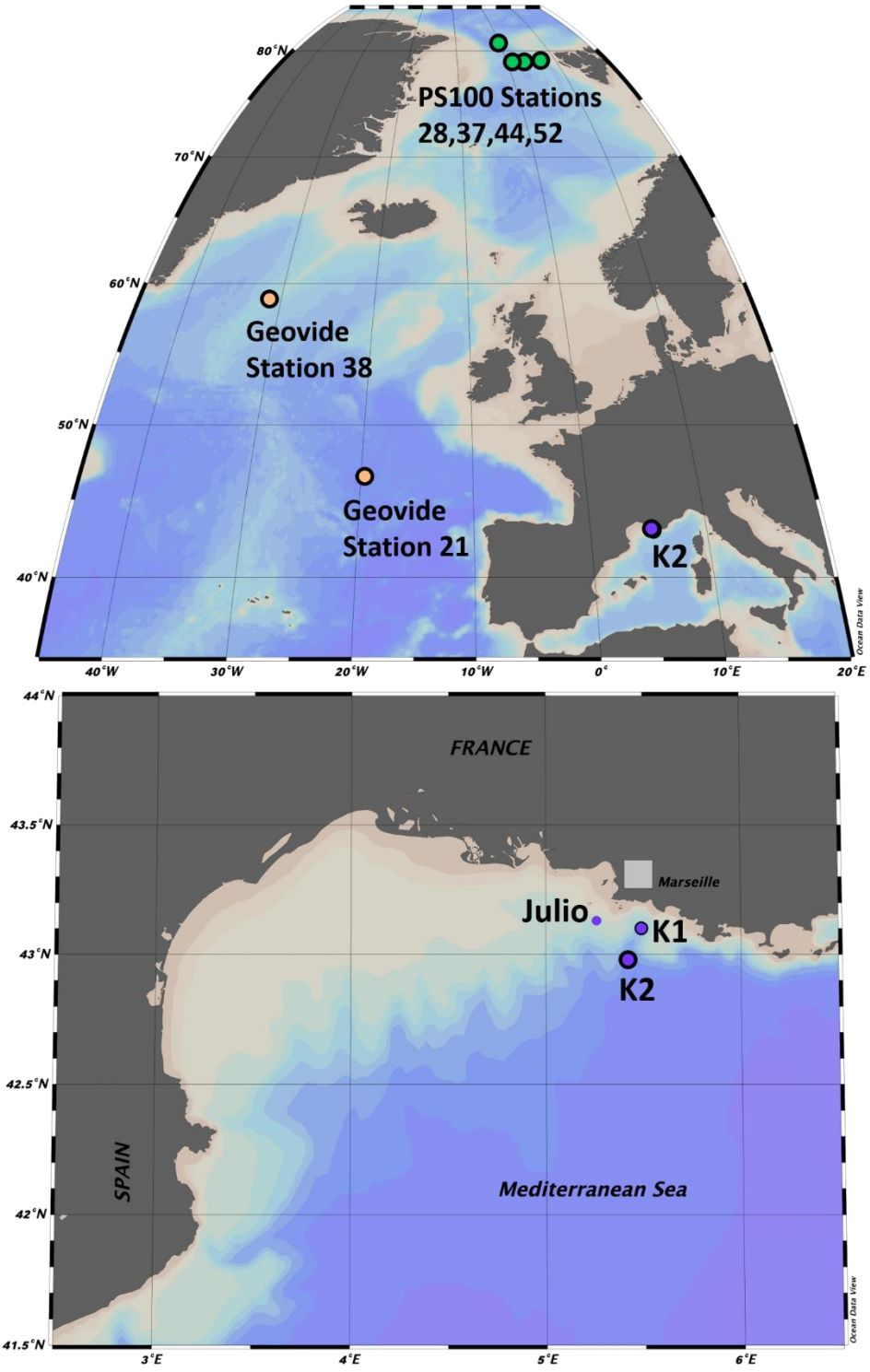

671

672 **Extended Data Figure 2. Maps of sampling locations for total and particulate Hg isotopes.** Top:
673 Sampling locations K2 in the Mediterranean Sea (purple), Atlantic Ocean (yellow) and Fram Strait
674 (green). Bottom: Zoom on the 4 Mediterranean locations, with main station K2 (large purple circle),
675 and pHg station K1 and Julio (small purple circles), and Endoume pier in Marseille Bay (grey square).
676 Maps were made with Ocean Data View (Schlitzer, Reiner, Ocean Data View, odv.awi.de, 2021)

677

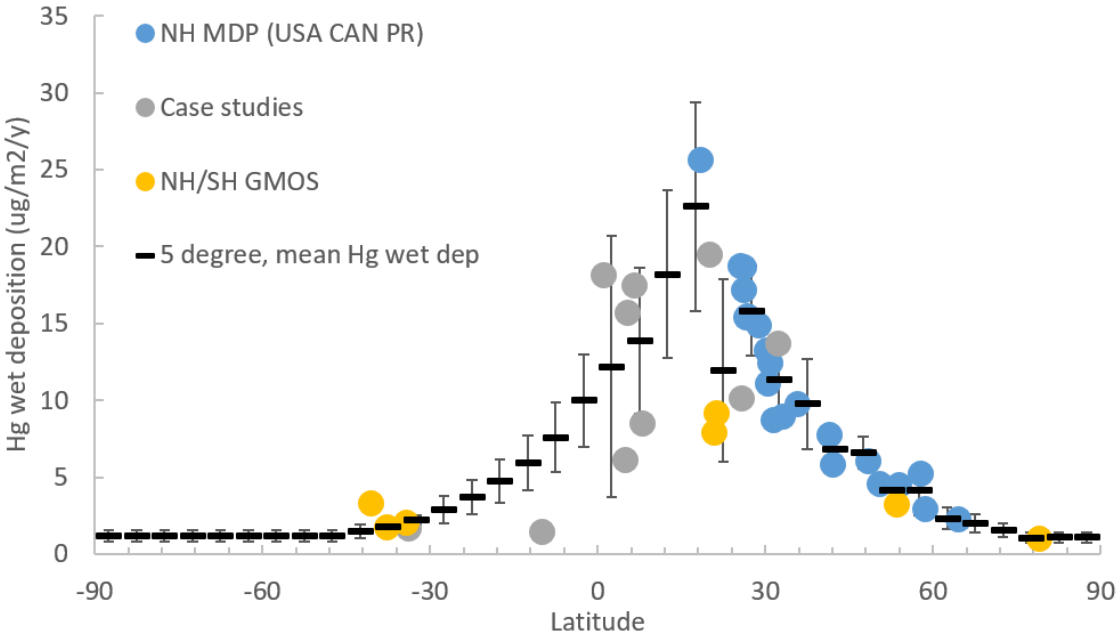

678

679 **Extended Data Figure 3. Latitudinal distribution of Hg(II) wet deposition.** Annual mean Hg(II) wet
680 deposition (µg m^{-2} y^{-1}) at oceanic locations in the northern and southern hemispheres (NH, SH), binned
681 in 5° latitude. Mean values (± standard deviation, SD) were calculated when sufficient data was
682 available per 5° latitude band, and interpolated using polynomial fitting when no data was available
683 (in which case a mean observed SD of 30% was applied). MDN, mercury deposition network; GMOS,
684 global mercury observation system; USA, CAN, PR, United States of America, Canada, Puerto Rico.

685

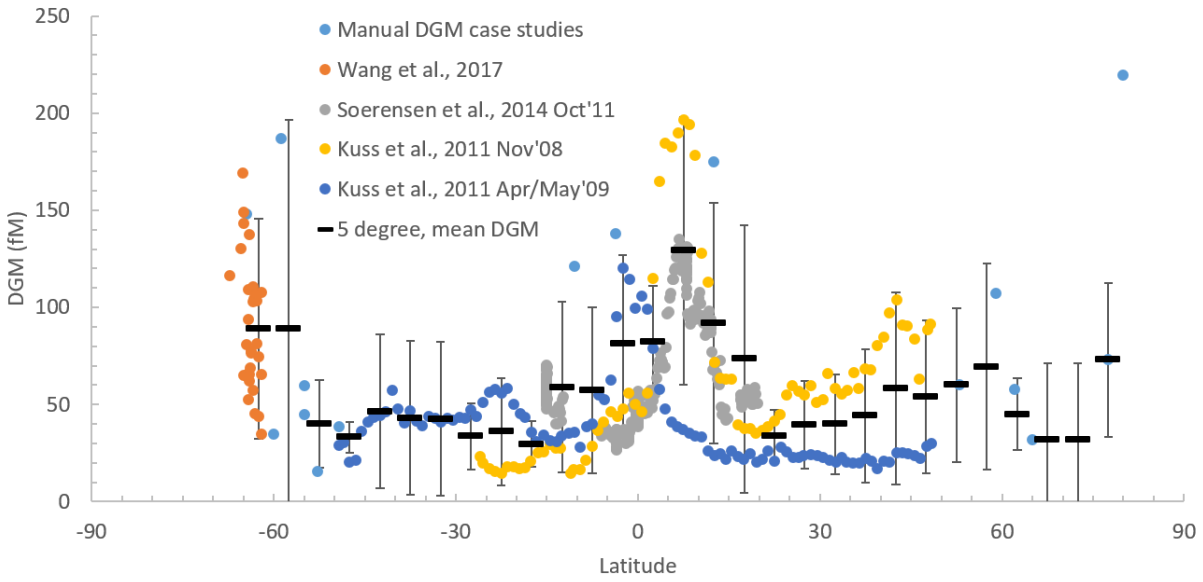

686

687 **Extended Data Figure 4. Latitudinal distribution of dissolved gaseous Hg (DGM) concentrations.**
688 Mean (± standard deviation) DGM are binned in 5° latitude bands, and equal weight was given to each
689 study. Polar studies, affected by sea ice show unusually high concentrations (mean 219 fM in the Arctic,
690 mean 138 fM around Antarctica) for high latitude waters and were excluded in 5° latitude binning
691 (replaced in calculations by 'open water only' DGM data at 55-60°S and 75-80°N).

692

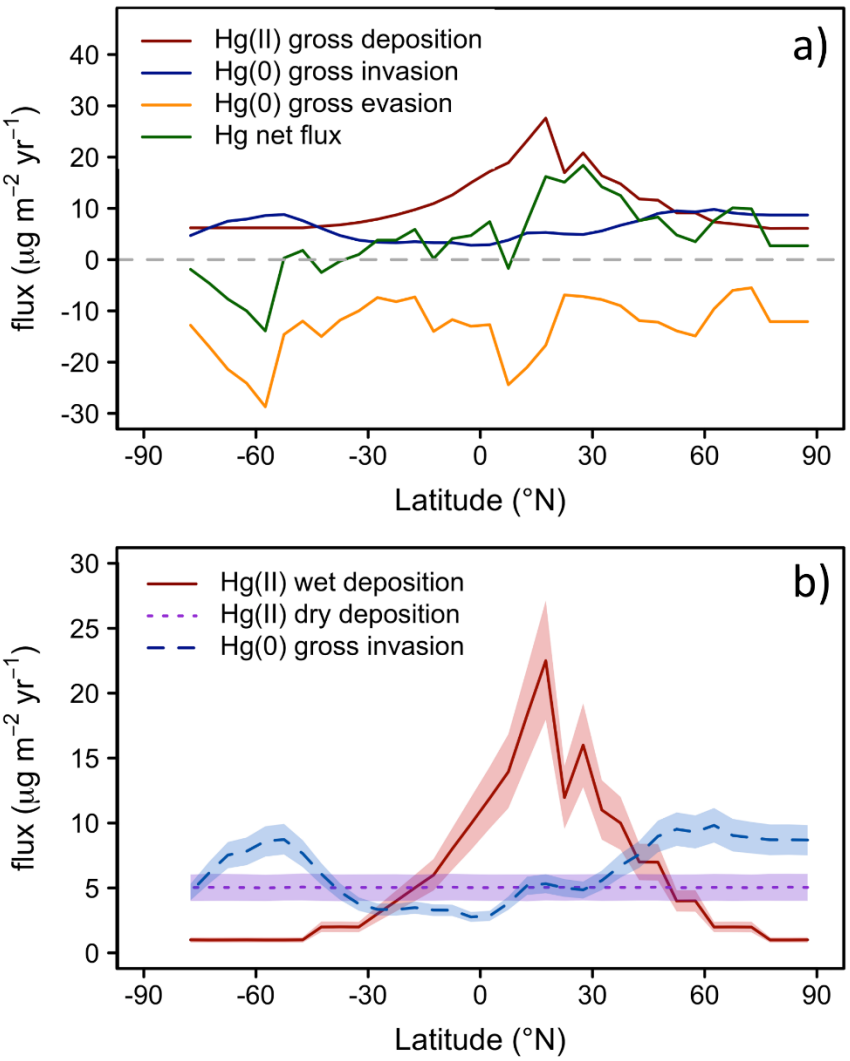

693

694 **Extended Data Figure 5. Atmospheric deposition pathways of the zonal 'Reference model'.** a): Marine
695 Hg(II) gross deposition, Hg(0) gross invasion, Hg(0) gross evasion, and net Hg flux [Hg(II) deposition +
696 Hg(0) invasion – Hg(0) evasion]; all in µg m^{-2} y^{-1} with evasion shown as negative numbers. Hg(0) invasion
697 is driven by observed atmospheric Hg(0) and wind speed. Hg(II) deposition is dominated by Hg(II) wet
698 deposition. Hg(0) evasion is driven by DGM concentrations and wind speed. The net Hg evasion trends
699 shows important net deposition in the northern hemisphere, and net evasion in the southern
700 hemisphere. b): 'Reference model' Hg gross deposition fluxes (µg m^{-2} y^{-1}) as a function of latitude used
701 in estimating marine Δ^{200}Hg in Figure 4a (main text). Hg(II) wet deposition observations as in Extended
702 Data Figure 3; Hg(II) dry deposition was fixed at 5 µg m^{-2} y^{-1}, and constrained as 40% of total Hg(II)
703 deposition[38], since no dry deposition observations over oceans exist. Hg(0) invasion (ocean uptake,
704 same as in top panel) is calculated from the observed inter-hemispheric atmospheric gaseous Hg(0)
705 gradient[3], wind and sea surface temperature (Copernicus), and the latest Hg(0) air-sea gas exchange
706 model (see SI text).

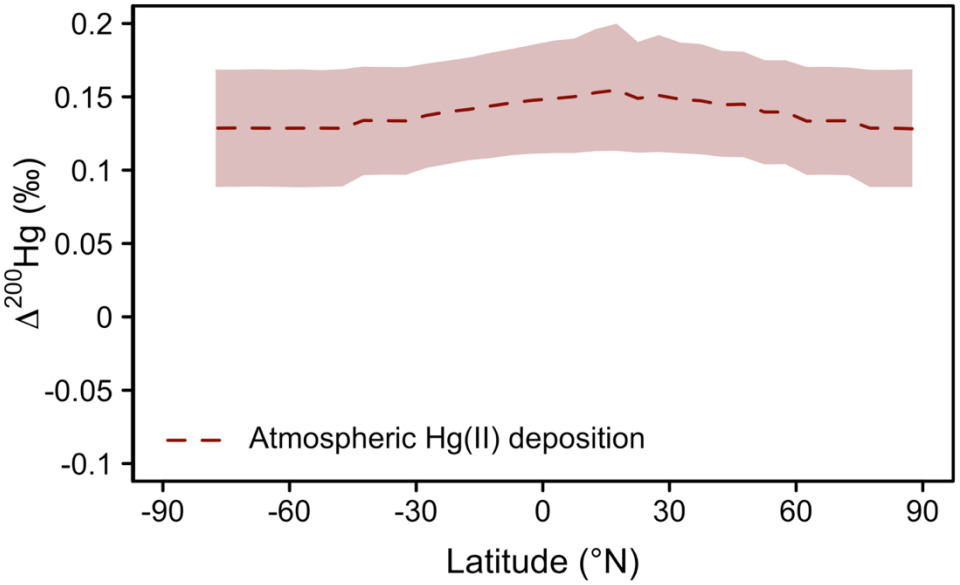

707

708 **Extended Data Figure 6: Estimated latitudinal variation in Δ^{200}Hg of atmospheric Hg(II) deposition.**
709 The small variation is caused by the variable contributions (Extended Data Figure 5) of Hg(II) wet
710 deposition with Δ^{200}Hg of 0.16‰, and Hg(II) dry deposition with Δ^{200}Hg of 0.10‰ (Extended Data Table
711 1). The dashed line represents the median and the shaded area the interquartile range (IQR).

712

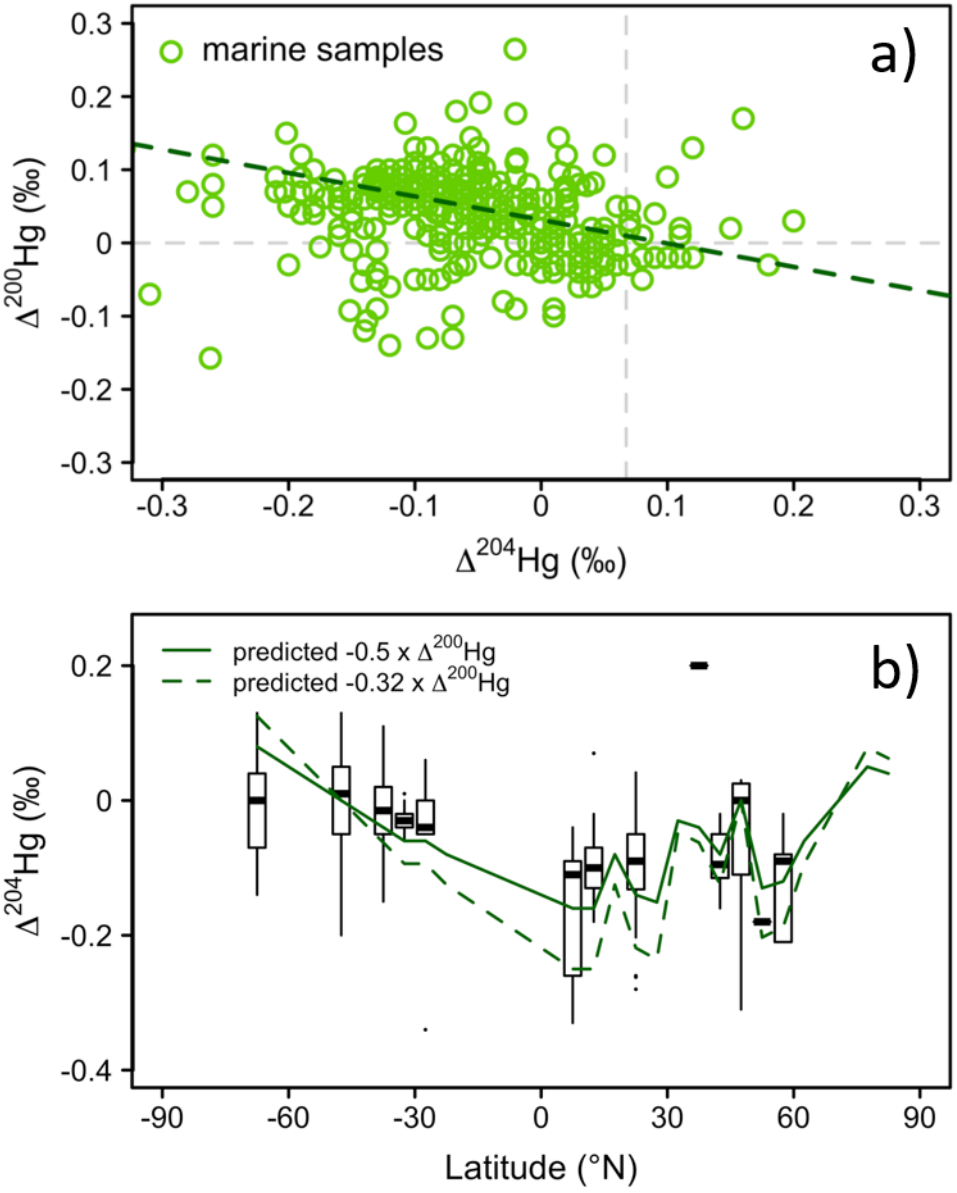

Extended Data Figure 7: Variation of Δ^{204}Hg in marine samples. a) Δ^{204}Hg vs Δ^{200}Hg. The dashed line represents the York regression using IsoplotR[57] for all marine samples (Δ^{200}Hg = -0.32(±0.06) Δ^{204}Hg + (0.03±0.004), (± se), MSWD = 0.213) b) Δ^{204}Hg boxplot for 5° latitudinal intervals. Marine samples are shown in boxes, where the bold horizontal line represents the median, the boxes the interquartile range, the whiskers 1.5 times the IQR and outliers are represented by dots. The solid line represents the predicted Δ^{204}Hg based on the observational relationship between Δ^{204}Hg and Δ^{200}Hg in terrestrial samples by Blum & Johnson, 2017[58]. The dashed line represents the predicted Δ^{204}Hg derived from the York regression shown in panel a). Δ^{204}Hg data are available for 339 out of 791 marine samples. Note that for pHg and tHg samples presented here, Δ^{204}Hg was not measured due to the low abundance of ^{204}Hg isotopes, and unavailability of a second 10^{13} Ohm amplifier.

724 **Extended Data Table 1: Summary of Hg stable isotope data.** *sediments considered below 1000m water depth. ND: not determined.

Pool	Ocean Basin	n	Hg concentration					δ^{202}Hg (‰)				Δ^{199}Hg (‰)				Δ^{200}Hg (‰)				References
			mean	median	p25	p75	units	mean	median	p25	p75	mean	median	p25	p75	mean	median	p25	p75	
Hg(II) rainfall		106	13.2	12.9	9	17.9	ng/L	-0.43	-0.30	-0.63	0.03	0.41	0.40	0.21	0.52	0.16	0.17	0.11	0.22	[23,24,30,40,59–63]
reactive Hg(II)		66	62.4	56.41	47.8	75.2	pg/m^3	-0.40	-0.55	-0.95	0.02	0.36	0.34	0.14	0.51	0.12	0.10	0.07	0.18	[27,40,41]
Atmospheric Hg(0)		220	1.38	1.265	1.1	1.57	ng/m^3	0.37	0.43	0.09	0.77	-0.19	-0.20	-0.25	-0.13	-0.06	-0.05	-0.08	-0.03	[23–25,42,64–66]
tHg	All samples	16	0.82	0.82	0.77	0.88	pM	-0.27	-0.24	-0.42	-0.04	0.08	0.06	0.02	0.11	0.02	0.02	-0.01	0.03	
	Med. Sea	12	0.89	0.83	0.80	1.01	pM	-0.17	-0.19	-0.32	0.07	0.07	0.06	0.01	0.09	0.01	0.01	-0.01	0.03	This study
	Atlantic	4	0.61	0.57	0.51	0.67	pM	-0.56	-0.45	-0.66	-0.36	0.11	0.09	0.04	0.16	0.05	0.06	0.02	0.09	This study
pHg	All samples	36	0.19	0.16	0.09	0.26	pM	-0.28	-0.23	-0.59	-0.10	-0.03	-0.03	-0.14	0.11	0.02	0.02	-0.02	0.06	
	Med. Sea	15	0.11	0.10	0.08	0.15	pM	-0.22	-0.12	-0.84	0.24	-0.06	-0.05	-0.13	-0.02	0.00	0.01	-0.03	0.05	This study
	Atlantic	9	0.31	0.28	0.24	0.32	pM	-0.61	-0.58	-0.73	-0.41	-0.21	-0.19	-0.27	-0.15	-0.02	-0.02	-0.03	0.01	This study
	Pacific	12	ND	ND	ND	ND	pM	-0.12	-0.14	-0.22	-0.11	0.16	0.16	0.11	0.18	0.06	0.06	0.05	0.07	[30]
sediment	All samples	92	83	52	32	84	ng/g	-0.99	-0.85	-1.21	-0.49	0.10	0.08	0.02	0.11	0.02	0.02	0.01	0.04	
	Med. Sea	40	66	53	44	83	ng/g	-1.28	-1.14	-1.61	-0.86	0.09	0.09	0.07	0.11	0.03	0.03	0.01	0.05	This study, [67,68]
	Atlantic	35	119	55	33	137	ng/g	-0.49	-0.40	-0.60	-0.33	0.01	0.00	-0.02	0.05	0.01	0.01	-0.01	0.03	[69,70]*
	Pacific	17	37	22	12	71	ng/g	-1.34	-0.95	-2.16	-0.66	0.29	0.31	0.21	0.34	0.04	0.03	0.02	0.05	This study
biota	All samples	643	2621	1360	450	3074	ng/g	0.78	0.75	0.31	1.20	1.66	1.60	1.31	1.86	0.04	0.05	0.02	0.08	
	Med. Sea	19	3131	2953	2460	3826	ng/g	0.36	0.37	0.29	0.47	1.76	1.78	1.70	1.82	0.07	0.07	0.05	0.08	This study
	Atlantic	74	1018	190	69	2240	ng/g	0.44	0.36	0.25	0.60	1.51	1.22	0.95	1.49	0.04	0.04	0.01	0.07	[71–74]
	Pacific	263	943	431	231	766	ng/g	0.45	0.45	0.07	0.85	1.61	1.47	1.13	1.85	0.06	0.07	0.04	0.08	[74–80]
	S. Ocean	287	3524	2129	930	3962	ng/g	1.20	1.21	0.81	1.55	1.74	1.68	1.55	1.90	0.03	0.03	0.00	0.07	[81–84]

725

726 **Extended Data Table 2: Modeled contribution of Hg(II) from wet and dry deposition**, $f_{Hg(II)}$, and excess
727 $\Delta^{199}Hg_{exc}$ according to Methods Equations 3, 4. Excess $\Delta^{199}Hg_{exc}$ represents sample $\Delta^{199}Hg$ acquired by
728 Hg(II) photoreduction in sea water, in addition to the $\Delta^{199}Hg$ inherited from atmospheric Hg deposition.

Pool	Ocean Basin	n	fHg(0)				$\Delta^{199}Hg_{exc}$ (‰)			
			mean	median	p25	p75	mean	median	p25	p75
tHg	All samples	16	0.61	0.58	0.50	0.76	0.04	0.00	-0.03	0.12
	Med. Sea	12	0.66	0.64	0.53	0.76	0.06	0.01	-0.03	0.14
	Atlantic	4	0.44	0.38	0.24	0.57	-0.03	-0.04	-0.07	0.00
pHg	All samples	36	0.60	0.58	0.39	0.82	-0.07	-0.05	-0.13	0.01
	Med. Sea	15	0.65	0.64	0.44	0.85	-0.08	-0.04	-0.17	0.00
	Atlantic	9	0.78	0.82	0.61	0.87	-0.15	-0.11	-0.17	-0.07
	Pacific	12	0.40	0.39	0.34	0.43	-0.01	-0.01	-0.08	0.07
sediment	All samples	92	0.58	0.57	0.49	0.65	0.03	0.03	-0.04	0.08
	Med. Sea	40	0.54	0.53	0.43	0.65	0.01	0.02	-0.05	0.05
	Atlantic	35	0.66	0.65	0.55	0.77	-0.01	0.00	-0.05	0.04
	Pacific	17	0.50	0.50	0.45	0.56	0.19	0.17	0.12	0.22
biota	All samples	643	0.47	0.40	0.31	0.60	1.55	1.52	1.19	1.75
	Med. Sea	19	0.35	0.33	0.31	0.39	1.56	1.58	1.50	1.65
	Atlantic	74	0.46	0.40	0.33	0.60	1.48	1.23	0.93	1.45
	Pacific	263	0.42	0.36	0.30	0.50	1.45	1.31	0.96	1.73
	S. Ocean	287	0.52	0.49	0.32	0.67	1.65	1.63	1.47	1.77

729

730

731 **Online Supporting Information to:**

732

733 Mercury stable isotopes constrain atmospheric sources to the Ocean

734 Martin Jiskra[1,2,*,#], Lars-Eric Heimbürger-Boavida[2,3*,#], Marie-Maëlle Desgranges[3], Mariia V. Petrova[3],
735 Aurélie Dufour[3], Beatriz Ferreira-Araujo[2], Jeremy Masbou[2], Jerome Chmeleff[2], Melilotus Thyssen[3],
736 David Point[2], Jeroen E. Sonke[2,#]

737 [1]Environmental Geosciences, University of Basel, Switzerland

738 [2]Géosciences Environnement Toulouse, CNRS/IRD/Université Paul Sabatier Toulouse III, France.

739 [3]Aix Marseille Université, CNRS/INSU, Université de Toulon, IRD, Mediterranean Institute of
740 Oceanography (MIO) UM 110, 13288, Marseille, France

741 *These authors contributed equally as 1st authors: M Jiskra, LE Heimbürger-Boavida

742 #Corresponding authors: martin.jiskra@unibas.ch, lars-eric.heimburger@mio.osupytheas.fr,
743 jeroen.sonke@get.omp.eu

744

745 Materials and Methods

746

747 Rationale

748 Total mercury (tHg) concentration in seawater is the sum of several operationally defined species,
749 including dissolved gaseous Hg(0), dissolved gaseous dimethyl-Hg (DMHg), dissolved inorganic Hg(II)
750 compounds, dissolved monomethyl-Hg compounds (MMHg), and particulate-bound Hg(II) and MMHg
751 compounds (pHg). Both concentration and stable isotope analysis of tHg in seawater require the
752 transformation of these compounds to dissolved, labile Hg(II) forms by addition of a strong oxidant
753 such as BrCl, prepared in concentrated HCl. The concomitant oxidation and acidification also inhibits
754 biological activity, stabilizes Hg(II) in solution and minimizes potential losses to sampling container
755 walls or to the atmosphere. Two criteria need to be met for a robust Hg stable isotope analysis of
756 seawater: first, the low-picomolar seawater concentration has to be concentrated to levels suitable
757 for Hg stable isotope analysis (typically 0.2 – 1 ng mL^{-1} or 1 – 5 nM). This pre-concentration needs to
758 be quantitative in order to avoid Hg isotope fractionation during transfer. Second, the procedural blank

of the method needs to be low, ideally below 10% of the total amount of Hg in the sample. Low blank levels rely on ultra-clean sampling at sea, clean sampling vessels and ultra-low Hg levels of reagents used.

Previous studies have successfully developed methods for large volume (1 - 20 L) pre-concentration of tHg from natural waters, including rain, snow, ice, lake and coastal seawater. Gratz et al. (2010) and Sherman et al. (2010) first used continuous cold vapor generation, with $SnCl_2$ as a reductant, to pre-concentrate 1 - 4 L of snow and rainfall samples into small volume (25 mL) 2 % (w/w) oxidizing $KMnO_4/H_2SO_4$ solution trap[1,2]. This method was later modified to a batch-reactor set-up to pre-concentrate 1 L of rainfall in a 2 L Pyrex bottle, by slow, pumped addition of $SnCl_2$, and identical $KMnO_4/H_2SO_4$ solution trap[3] and trapping solutions of 40 vol% inverse *aqua regia* (iAR, 4.2 N HNO_3, 1.2 N HCl)[4]. Finally, in Obrist et al. (2017) we scaled up the batch purge and trap method to handle up to 20 L of snow and rain sample[5]. An alternative method was developed by Chen et al. (2016) using the AG-1-X4 anion exchange resin to pre-concentrate >40 ng of tHg from freshwater lakes[6]. $HgCl_4^{2-}$ in the acidified, 0.1 N HCl, sample is pumped at 3.5 mL min^{-1} over 0.5 mL of AG-1-X4 resin. Sorbed Hg is then eluted with 10 mL of 0.05 % L-cysteine in 0.5 N HNO_3, oxidized by BrCl, neutralized with NH_4OH and analyzed by MC-ICPMS. Štrok et al. (2015) optimized the anion exchange resin method for seawater and published the first Hg stable isotope data of coastal seawater (1.5-3.1 pM) from the Canadian Arctic Archipelago[7]. The latter two methods by Štrok et al. (2015) and Obrist et al. (2017) are capable of handling sample volumes of 20 L or more that are necessary for background level tHg pre-concentration from seawater (0.4 to 1.5 pM). Our objective was therefore to adapt our existing large volume pre-concentration protocol, based on $SnCl_2$ reduction, for rain and snow to seawater. We optimized the protocol for quantitative pre-concentration yields and low blank levels.

Pre-concentration troubleshooting, Sn waste disposal and bottle cleaning

During pre-concentration the 20L sample bottle is under argon over-pressure in order to generate a fine stream of bubbles. It is therefore important at the end of pre-concentration, or during troubleshooting, not to vent the argon supply tube to the 20L sample bottle and release argon pressure. The reason is that with the 20 L bottle under over-pressure, venting the argon supply tube results in a sudden pressure drop, and acidified sample solution with $SnCl_2$ moving from the 20 L bottle into the tall bubbler post, possibly all the way to the argon flow regulator, damaging the latter. Worse, the 40 vol% iAR trap solution is aspirated up into its short bubbler post and into the 20 L bottle, resulting in the loss of the sample. Using our final optimized Sn addition protocol, each 20 L bottle

791 contains at the end of a pre-concentration run, 2.5 g of Sn(II), and should be disposed of following local
792 environmental regulations. If needed, the dissolved Sn(II) concentration can be lowered by hydrogen
793 peroxide addition, which quantitatively precipitates $Sn(IV)O_2$, that can then be filtered or decanted.
794 Quantitative oxidation of Sn(II) by hydrogen peroxide also has the advantage that no traces of Sn(II)
795 remain in the 20 L bottle, which can be acid-cleaned (0.1 vol% commercial HCl) and rinsed with
796 abundant MQ water to receive the next batch of seawater samples. In this study both sampling and
797 pre-concentration were done in the same bottle. We expect however that the use of separate bottles,
798 possibly using plastic 20 L carboys at sea for safety, does not increase blanks.

799

800 **Alternative, activated carbon based pre-concentration method for sea water**

801 We have, over the past years, tested an alternative method for low-level Hg pre-concentration in order
802 to measure Hg isotopes in sea water. The method uses small 200 mg iodated activated carbon powder
803 (Brooks Rand) cartridges, over which large volumes (50L) of unfiltered, acidifed (0.4% v/v HCl) sea
804 water are pumped at a slow flow rate of 5 ml min^{-1}. Following laboratory recovery and blank testing,
805 we applied the method during the 2014 GEOTRACES Geovides cruise in the North-Atlantic Ocean.
806 Unfiltered seawater was transferred using clean 6mm FEP tubing from GOFLO bottles into acid washed
807 50L tedlar bags. A peristaltic pump, with 1.14mm ID (red/red) tygon pump tubing was used to load
808 samples on the IAC traps during 1 week. Traps were dried for 5 min in a dry high purity argon stream,
809 sealed with silicone stoppers and stored and transported dry and in the dark to the GET laboratory.
810 The IAC powder was combusted using a dual tube furnace combustion method[8]. IAC blanks were 0.5
811 ng Hg per 200mg of IAC traps, and sample recoveries were 88 ± 31%. In hindsight, it has been difficult
812 to fully recover Hg from IAC traps due to abundant volatile iodine release and transfer to oxidizing
813 solution traps. We recommend that further development of activated carbon based methods use
814 commercial sulfur impregnated activated carbon (Calgon HGR), which does not have this issue[9].

815

816 **MMHg and DMHg analysis**

817 MMHg and DMHg were determined by isotope dilution (ID)- gas chromatography – sector field ICP-
818 MS (ID-GC-SF-ICPMS) method at the MIO laboratory, following previously published protocols[10]. First
819 the sum of both species (tMeHg) was quantified on an acidified sample that converts DMHg to MMHg.
820 A second replicate sample was purged to remove DMHg before acidification, allowing direct
821 measurement of MMHg. DMHg was calculated by difference, as tMeHg – MMHg. In both sample

aliquots MMHg and inorganic Hg species were extracted after derivatization. In brief, enriched spikes of ^{199}iHg and ^{201}MeHg (ISC Science, Spain) were added to a 115 mL aliquot of the sea water samples. After 24h of equilibration, pH was adjusted to 3.9 with NH_3 (ULTREX® II Ultrapure Reagent, J.T. Baker, USA) and a buffer solution made up with acetic acid (glacial, ULTREX® II Ultrapure Reagent, J.T. Baker, USA) / sodium acetate (J.T. Baker, USA). A solution of 1 % (v:v) sodium tetra propyl borate (Merseburger Spezialchemikalien, Germany) was made up freshly, under cold conditions and avoiding contact with atmospheric oxygen. 1 mL of this solution was then added together with 200 µL hexane (Sigma Aldrich, USA). The glass bottles were hermetically sealed with Teflon-lined caps and vigorously shaken for 15 minutes. The organic phase was recovered and injected in the GC (Thermo Trace Ultra), coupled to a sector field ICPMS (Thermo Element XR). Detection limits were 0.005 pM for MMHg, and 0.01 pM for DMHg.

pHg isotope results

At station K2, pHg Δ^{199}Hg and Δ^{200}Hg were similar in June 2017 and May 2019 at all depths, while δ^{202}Hg was higher in June 2017 by 1.5 ‰ at 100 - 400m depth. Only in May 2019 at station K2, tHg and pHg isotopes were determined simultaneously and δ^{202}Hg of pHg was depleted by -1.0 ‰ (-0.8 ‰ to -1.3‰; median and (IQR), n = 4) relative to tHg (Figure 1b). Light isotope enriched pHg may be explained by the preferential sorption of light Hg(II) isotopes to particulate organic matter[11], or by preferential uptake of light isotopes by phytoplankton that is part of the particulate pool. pHg stable isotopes sampled in 2017 at two stations, Julio and K1, closer to the coast were similar to the open sea station (K2) with no clear trends in water depth or distance from the shore (Figure S1). Marine sediments, analyzed for station Julio only (700 m depth), had similar δ^{202}Hg = -0.75 ‰ (-0.76 to -0.74 ‰), Δ^{199}Hg = 0.05 ‰ (0.04 to 0.05 ‰) and Δ^{200}Hg = 0.03 ‰ (0.00 to 0.06 ‰) (median and (IQR), n = 4) to mean water column pHg (K1, K2, Julio), and were similar to sediment samples taken elsewhere in the Mediterranean Sea[12,13].

Sea water Δ^{199}Hg and photochemical reduction of Hg(II) to Hg(0)

During photoreduction of Hg(II)-organic ligand complexes the magnetic isotope effect (MIE) may separate even from odd Hg isotopes[14]. Experimental photomicrobial Hg(II) reduction in simulated sea water medium has been shown to lead to negative Δ^{199}Hg in residual aquatic Hg(II)[15]. The sign (positive, negative Δ^{199}Hg) and magnitude of the MIE is not fully understood, but has been shown to depend on

853 the nature of the Hg-binding ligand (e.g. O or S), the Hg to ligand concentration ratio, and
854 environmental conditions such as pH[16,17]. Here, we evaluate whether the tHg and pHg data show
855 evidence of in situ marine odd-MIF, in addition to that inherited from atmospheric deposition sources.
856 We first calculate the excess $\Delta^{199}Hg_{exc}$ in all seawater samples, defined as the difference between the
857 measured $\Delta^{199}Hg$ in a marine sample and the expected $\Delta^{199}Hg$, based on atmospheric inputs. The
858 expected $\Delta^{199}Hg$ was calculated by binary mixing of $\Delta^{199}Hg$ in atmospheric Hg(II) and Hg(0) using the
859 source contributions (fHg(II)) derived from $\Delta^{200}Hg$ (Methods, equation 3). The excess $\Delta^{199}Hg$ in the
860 different marine Hg pools ($\Delta^{199}Hg_{exc}$), representing the $\Delta^{199}Hg$ which was produced within the marine
861 system, was calculated as follows:

862 $$\Delta^{199}Hg_{exc} = \Delta^{199}Hg_{meas} - (f_{Hg(II)} \times \Delta^{199}Hg_{Hg(II)} + (1- f_{Hg(II)}) \times \Delta^{199}Hg_{Hg(0)}) \quad \text{(Eq. S1)}$$

863 , where $\Delta^{199}Hg_{meas}$ is the measured value. Overall, the $\Delta^{199}Hg$ pattern in tHg and pHg of seawater and
864 marine sediments is similar to $\Delta^{200}Hg$ and observed $\Delta^{199}Hg$ can largely be explained by a conservative
865 mixing of atmospheric Hg(0) and Hg(II) deposition (Figure 2B and 3B). Atlantic and Mediterranean
866 $\Delta^{199}Hg_{exc}$ was 0.03‰ (0.02 to 0.13‰; median, inter quartile range (IQR), n = 17) in tHg and 0.01‰ (-
867 0.07‰ to 0.08‰; median, IQR, n = 61) in pHg, which is not significant. Very low $\Delta^{199}Hg_{exc}$ were also
868 found in marine sediments of the Mediterranean Sea (0.09‰, 0.03‰ to 0.12‰) and the Atlantic
869 Ocean (0.06‰, 0.02 to 0.10‰). Elevated median $\Delta^{199}Hg_{exc}$ of 1.64‰ in marine fish (Extended Data
870 Table 2) can therefore be predominantly ascribed to photochemical breakdown of MMHg. The absence
871 of significant odd-MIF in surface seawater does not automatically mean that photoreduction is slow,
872 or that the MIE is absent. Experimental photoreduction observations on seawater, under
873 representative conditions, are needed to examine the issue.

874

875 **Observation-based estimates of global marine Hg(II) deposition, and air-sea Hg(0) exchange as a**
876 **function of latitude**

877 In order to assess potential latitudinal bias in the global $\Delta^{200}Hg$ mass balance (main text), which for tHg
878 and pHg is mostly based on northern hemisphere mid-latitude $\Delta^{200}Hg$ observations (43°-81°N), we
879 perform in this section a full 5 degree zonal analysis of marine $\Delta^{200}Hg$, rainfall Hg(II), dissolved gaseous
880 Hg(0), climatology and calculated Hg(0) invasion, and evasion fluxes as a function of latitude. The
881 analysis is based on 1. A review of marine aqueous, pelagic biota and pelagic sediment $\Delta^{200}Hg$, 2. A
882 review of the latitudinal distribution of Hg(II) wet deposition, 3. A review of gross Hg(0) invasion (i.e.
883 ocean uptake), which allows us to estimate, by mass balance, an expected $\Delta^{200}Hg$ gradient which we
884 compare to observed marine $\Delta^{200}Hg$, and 4. A reversed mass balance where we use the observed

885 marine Δ^{200}Hg gradient to estimate the ocean Hg(0) uptake flux, or the Hg(II) deposition that is needed
886 to explain the Δ^{200}Hg observations.

887 1. Figure S3 (and Figure 4, main text) shows the latitudinal distribution of marine pelagic Δ^{200}Hg.
888 Δ^{200}Hg of marine data at high latitudes (>60°, 0.01 ‰ (-0.04 ‰ to 0.03‰); median and IQR, n= 69) in
889 both hemispheres are significantly lower ($p<0.001$, one-sided t test), than mid-latitude (30-60°, 0.03 ‰
890 (0.01 ‰ to 0.065‰); median and IQR, n= 428), which are significantly lower ($p<0.001$, one-sided t test)
891 than the (sub)tropics (0-30°, 0.07 ‰ (0.04 ‰ to 0.085‰); median and IQR, n= 275). This trend suggests
892 that Hg(II) and Hg(0) deposition contributions to pelagic marine waters are variable. The trend also
893 confirms, to first order, that the observed higher Δ^{200}Hg (0.06 ‰) in sub-tropical pHg (Motta et al.,
894 2019)[18] and lower pHg Δ^{200}Hg in mid-latitude (0.01 ‰) and high latitude (-0.02 ‰) waters (this study)
895 are coherent features that belong to a broader latitudinal trend in marine Δ^{200}Hg.

896 2. We review Hg(II) wet deposition at remote coastal and island monitoring sites globally, and
897 during a S-Atlantic cruise[19] that collected a large number of rainfall events (Extended Data Figure 3,
898 n=12,812). We find a gradual increase from 1.7 ± 0.9 μg m^{-2} y^{-1} at high latitudes to 6.7 ± 4.0 at mid-
899 latitudes to 15 ± 5 in the (sub-)tropics (mean ± sd), generally attributed to convective cloud formation
900 and upper tropospheric Hg(II) scavenging[20]. Whereas the northern hemisphere (NH) (sub-)tropical
901 rainfall Hg(II) maximum is well defined for Mercury Deposition Network (MDN[21]) sites along the coastal
902 N-Atlantic Ocean and Caribbean seas, only limited data is available for the NH Southeast Asian seas[22,23],
903 the Pacific Ocean at Hawaii[18], the equator[19,24,25] and the southern hemisphere (SH)[19,26,27]. Extrapolation
904 of the latitudinal Hg(II) wet deposition trend at marine locations to the global Ocean gives a Hg(II) wet
905 deposition flux of 2561 ± 768 Mg y^{-1}, assuming the relative standard deviation of 30% observed for
906 individual 5° latitude intervals applies at the global scale. Seasonal Hg(II) dry deposition observations
907 over oceans are inexistent, and must be estimated from 3D Hg models. Model Hg(II) wet deposition
908 generally is on the order of 60% of total Hg(II) deposition, the remaining 40% being Hg(II) dry
909 deposition[28,29]. For the observed global Hg(II) wet deposition budget of 2561 Mg y^{-1}, Hg(II) dry
910 deposition would then correspond to 1615 ± 485 Mg y^{-1}. In the absence of observations, we assume
911 Hg(II) dry deposition to be constant as a function of latitude at 5 μg m^{-2} y^{-1}, which respects its
912 contribution of 40% to modeled global Hg(II) deposition. The hybrid observational-model estimate
913 (indicated as zonal 'reference model in main text, and Figures 4, Extended Data Figure 5) of global
914 Hg(II) deposition to oceans of 4268 ± 1280 Mg y^{-1} is therefore similar to atmospheric Hg(II) deposition
915 of 4600 Mg y^{-1} in Hg cycling models[29]. Both our zonal 'reference model' and 3D Hg cycling models rely
916 heavily on coastal and continental rainfall observation sites, in particular from the MDN network in N-
917 America. It is therefore possible that the coastal rainfall observations, despite our pre-selection of non-

urban remote sites, are biased high by regional anthropogenic Hg(II) emissions. Consequently the marine Hg(II) deposition budget discussed here (Extended Data Figure 3) may therefore be biased high, which we argue (in the main text discussion) is a potential reason for the Δ^{200}Hg-based underestimation of Hg(0) to the marine Hg budget in 3D Hg cycling models.

3. We review surface Ocean dissolved gaseous Hg (DGM) measurements in order to estimate mean latitudinal DGM distribution (Extended Data Figure 4), and a DGM observation-based global marine Hg(0) gross and net emission budget. While DGM technically includes both dissolved gaseous Hg(0) and DMHg, it is thought to represent mostly Hg(0) due to the low surface ocean DMHg concentrations. We estimate marine Hg(0) evasion based on marine boundary layer atmospheric gaseous Hg(0) distribution[30]. We use latitudinal mean DGM, mean annual sea surface temperature (SST; 2007-2019; Copernicus product WIND_GLO_PHY_CLIMATE_L4_REP_012_003), wind speed at 10m above sea level (μ_{10}; 2007-2019; Copernicus product SST_GLO_SST_L4_NRT_OBSERVATIONS_010_001), and marine boundary layer Hg(0), to calculate global gross Hg(0) invasion (F_{inv}, Eq S2), gross evasion (F_{ev}, Eq S3) and net Hg(0) evasion (F_{net}, Eq S4) for 5^o latitude bands (all in ng m^{-2} h^{-1}) as follows:

$$F_{inv} = K_w \times -C_a/K_H \quad \text{(Eq. S2)}$$

$$F_{ev} = K_w \times C_w \quad \text{(Eq. S3)}$$

$$F_{net} = K_w \times (C_w - C_a/K_H) \quad \text{(Eq. S4)}$$

where C_w is the surface sea water DGM concentration (ng m^{-3} sea water), C_a is the air Hg(0) concentration (ng m^{-3} air), K_H is the dimensionless Henry's law constant, and K_w is the Hg(0) gas transfer velocity (m h^{-1}):

$\ln(K_H) = 2403.3/T+6.92$ from Andersson et al. 2008[31], where T is the SST in degrees Kelvin

$K_w = 0.25 \times \mu_{10}^2 \, (Sc_{Hg0}/Sc_{CO2})^{-0.5}$ from Nightingale et al. 2000[32], where Sc_{Hg0} is the Schmidt number for Hg(0):

$Sc_{Hg0} = v/D$

where v is the kinematic viscosity ($cm^2\ s^{-1}$) = 0.027 x $e^{(-0.025 \times T')}$ with T' the SST temperature in degrees Celsius, and D, the diffusivity of Hg(0) in sea water ($cm^2\ s^{-1}$) = 0.02293 x $e^{-(17760\ J/mol)/RT}$, where R is the Boltzman's constant (8.314 J K^{-1} mol^{-1}), and T is SST in Kelvin, all based on Kuss et al. 2009[33].

Hg(II) deposition, gross Hg(0) invasion, gross Hg(0) evasion and net Hg evasion as a function of latitude are summarized in Extended Data Figure 5 top. Hg(0) invasion is driven by observed atmospheric Hg(0) and wind speed and is maximal at mid and high latitudes. Hg(II) deposition is dominated by Hg(II) wet deposition in the sub-tropical NH. Hg(0) evasion is driven by high DGM concentrations in the (sub-)tropics (Extended Data Figure 3) and by high wind speed at mid and high latitudes. The net Hg evasion trend shows important net deposition in the northern hemisphere, and net evasion in the southern hemisphere, in agreement with 3D Hg cycling models[29] and observations[34]. We use Hg(II) wet deposition, Hg(II) dry deposition and Hg(0) invasion estimates (Extended Data Figure 5 bottom), together with Δ^{200}Hg end-members (Extended Data Figure 6, Extended Data Table 1, Equation 3) to calculate an expected latitudinal marine, pelagic Δ^{200}Hg distribution (Figure 4a). Expanded uncertainties on Δ^{200}Hg are estimated using a Monte Carlo script in R by randomly varying the stated uncertainties on fluxes and end-member Δ^{200}Hg. Due to the asymmetric latitudinal contributions of Hg(II) deposition and Hg(0) invasion to marine Hg, the expected Δ^{200}Hg trend (Figure 4a, main text) shows lower values at high latitudes and maximum, positive values in the NH (sub-)tropics. The observed marine Δ^{200}Hg distribution is significantly lower than the predicted Δ^{200}Hg distribution, except between 45 – 65°N (Figure 4). Our new tHg Δ^{200}Hg observations in the Mediterranean Sea and Atlantic Ocean between 43 – 59°N are therefore coherent with predicted Δ^{200}Hg. The majority of marine Δ^{200}Hg observations, however, are lower than the predicted Δ^{200}Hg, which leads us to conclude that the contribution of atmospheric Hg(0) to the oceans and to marine biota is underestimated.

Although we were not able to measure the Δ^{204}Hg in tHg and pHg, due to instrumental limitations (minor isotope, only one 10^{13} Ohm amplifier available and attributed to ^{198}Hg), the large marine biota and sediment data set contains abundant Δ^{204}Hg observations. In Extended Data Figure 7 we show that these data are consistent with Δ^{200}Hg observations in the same marine biota data, and with the Δ^{200}Hg:Δ^{204}Hg relationship observed in terrestrial samples[35].

4. Above we used a hybrid approach combining observations of Hg(II) wet deposition and atmospheric Hg(0), and 3D model-based Hg(II) dry deposition and Hg(0) gas-exchange to predict marine Δ^{200}Hg. The predicted Δ^{200}Hg trend is shifted to higher values compared to observed marine Δ^{200}Hg. Here we discuss why the zonal model, and 3D Hg cycling model predicted Hg(II):Hg(0) gross deposition ratio of 3:1 overestimates Hg(II) deposition to oceans. It is important to understand that Δ^{200}Hg does not inform on the absolute magnitude (in μg m^{-2} y^{-1}, or in Mg y^{-1}) of Hg(II) deposition and

978 Hg(0) uptake fluxes. Rather, it informs on the relative Hg(II) and Hg(0) contributions, and therefore
979 constrains the ratio of the marine Hg(II):Hg(0) gross deposition flux. We therefore need to ask which
980 of the two (or both) absolute flux estimates, either per 5^{o} latitude band, or on a global basis, is biased.
981 We have indicated above that the marine Hg(II) wet deposition flux is mostly observed at coastal N-
982 American stations, and only rarely over the open Ocean. Using a fitting approach, minimizing the root
983 mean square error (rmse) between observed and predicted Δ^{200}Hg, we estimate that Hg(II) wet
984 deposition would need to be approximately half (1252 Mg/y) the current estimate (2561 ± 768, 1SD)
985 to achieve a good fit (Figure 4d, main text). Note that if marine Hg(II) wet deposition is 100% lower,
986 then automatically Hg(II) dry deposition, fixed at 40% of total Hg(II) deposition also becomes 100%
987 lower. With respect to the GEOS-Chem budget, Hg(II) deposition would need to be lowered 2.7x from
988 4600 to 1700 Mg y^{-1} in order to achieve a 1:1 Hg(0):Hg(II) gross deposition ratio. We consider that 2-
989 3x times lower Hg(II) deposition is plausible, given the overall uncertainty on observations, and given
990 that the latitudinal coastal Hg(II) wet deposition distribution is asymmetric with higher deposition in
991 NH Hg emission source regions.

992 We can also keep Hg(II) deposition constant, and increase ocean Hg(0) uptake by increasing
993 the gas-transfer velocity, K_w in equations S1-S3, by a factor of 2.3 to achieve an optimum fit between
994 observed and predicted Δ^{200}Hg (Figure 4d, main text). In GEOS-Chem, K_w would have to be increased
995 270% to increase Hg(0) evasion from 1700 to 4600 Mg y^{-1}. A 230 - 270% increase in K_w exceeds the
996 typical uncertainty on Hg(0) gas-exchange models which is on the order of 30%[36,37]. However, since the
997 Hg(0) gas-exchange parameterizations are extrapolated from CO_2, they have not been calibrated
998 against experimental or field observations. In particular the effects of surface ocean micro-layer
999 chemical reactions, for example by consumption of invading Hg(0), could cause underestimation of K_w.
1000 However, there is a caveat in fitting K_w to optimize ocean Hg(0) uptake: gross marine Hg(0) emission
1001 and net marine Hg(0) exchange also depend linearly on K_w (equations S2, S3). A 230% increase in K_w
1002 would result in large global gross marine Hg(0) emission (10900 Mg/y) and large net air-sea Hg(0)
1003 exchange (6500 Mg/y) fluxes. A larger net exchange flux would change the ocean from a net sink in
1004 present Hg cycling models, to a net source, which would have to be balanced by an additional
1005 terrestrial sink to keep the atmosphere in steady state (as observed).

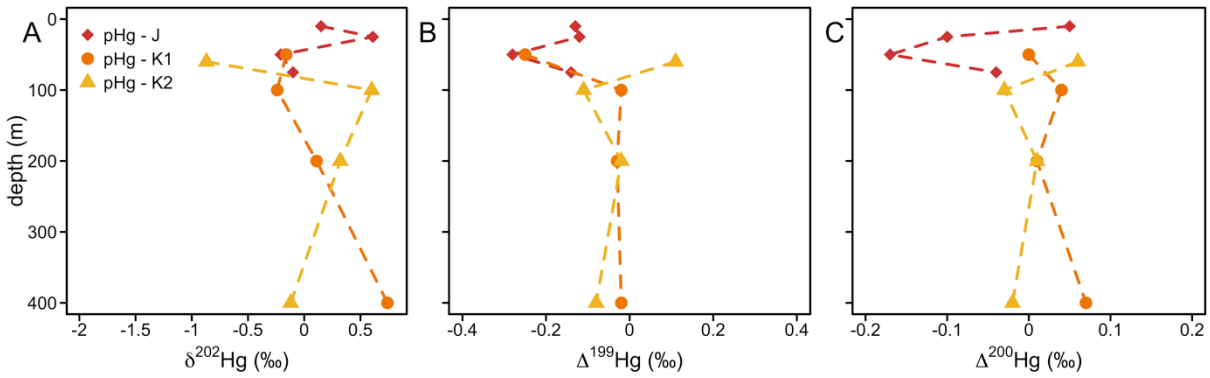

1006

1007 Figure S1. Depth profile of particulate Hg stable isotope composition at three stations in the
1008 Mediterranean Sea during the June 2017 campaign. A: mass-dependent fractionation (δ^{202}Hg), B: odd
1009 mass-independent fractionation (Δ^{199}Hg), C: even mass-independent fractionation (Δ^{200}Hg).

1010

1011

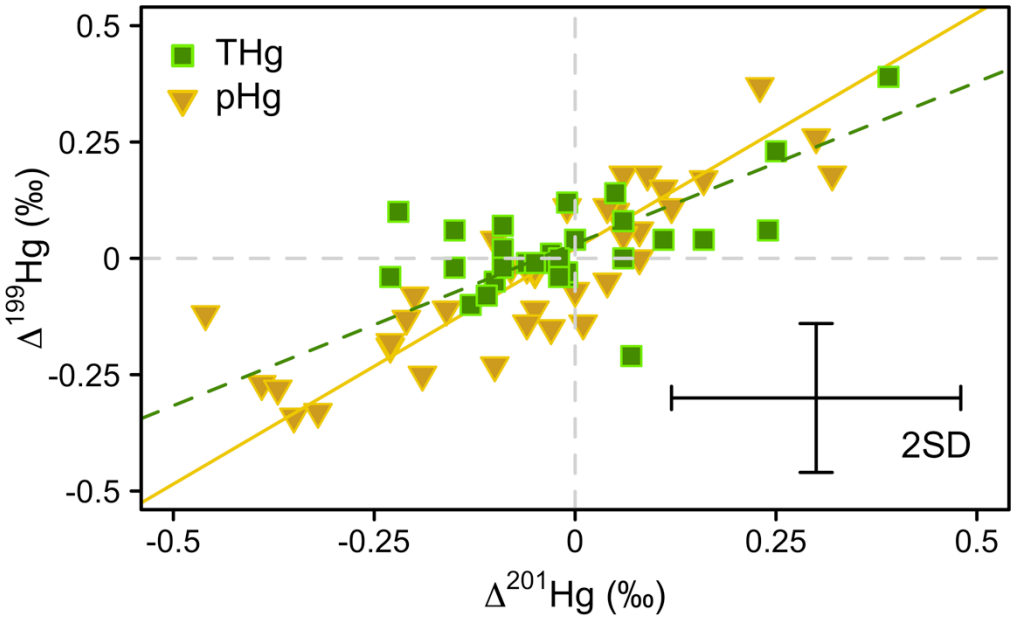

1012

1013 Figure S2: Scatterplot of odd Hg isotope mass-independent fractionation, Δ^{201}Hg vs. Δ^{199}Hg of all tHg
1014 and pHg seawater data, including the published data by Motta et al. 2019. The dashed line
1015 represents the York regression using IsoplotR[38] for tHg (Δ^{199}Hg = 0.79(±0.29) Δ^{201}Hg + (0.03±0.04), (±
1016 se), MSWD = 0.2). The solid line represents the York regression for pHg (Δ^{199}Hg = 1.01(±0.0.09)
1017 Δ^{201}Hg + (0.02±0.02), (± se), MSWD = 1.25). Error bars represent the 2 SD of replicate procedural
1018 standards for tHg and pHg.

1019

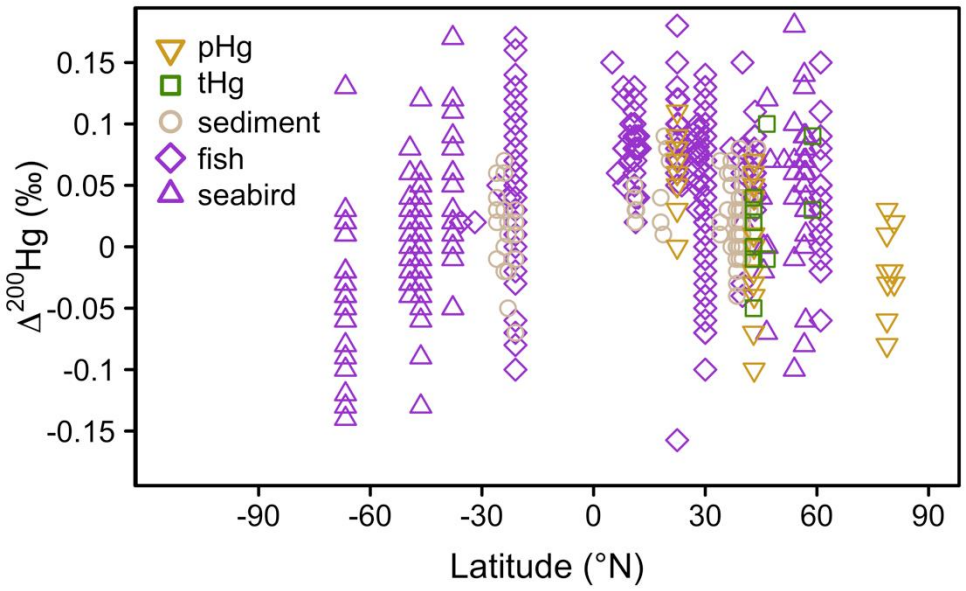

1020

1021 Figure S3: Variation of even-MIF Hg stable isotope composition (Δ^{200}Hg) in 787 individual marine
1022 samples resolved by sample type as function of latitude. See Extended Data Table 2 for data sources.

1023

SI References

1. Gratz, L., Keeler, G., Blum, J. & Sherman, L. S. Isotopic composition and fractionation of mercury in Great Lakes precipitation and ambient air. *Environmental Science and Technology* **44**, 7764–7770 (2010).
2. Sherman, L. S. *et al.* Mass-independent fractionation of mercury isotopes in Arctic snow driven by sunlight. *Nature Geoscience* **3**, 173–177 (2010).
3. Sherman, L. S., Blum, J. D., Keeler, G. J., Demers, J. D. & Dvonch, J. T. Investigation of Local Mercury Deposition from a Coal-Fired Power Plant Using Mercury Isotopes. *Environmental Science & Technology* **46**, 382–390 (2012).
4. Enrico, M. *et al.* Atmospheric mercury transfer to peat bogs dominated by gaseous elemental mercury dry deposition. *Environmental Science & Technology* (2016) doi:10.1021/acs.est.5b06058.
5. Obrist, D. *et al.* Tundra uptake of atmospheric elemental mercury drives Arctic mercury pollution. *Nature* **547**, 201-+ (2017).
6. Chen, J., Hintelmann, H. & Dimock, B. Chromatographic pre-concentration of Hg from dilute aqueous solutions for isotopic measurement by MC-ICP-MS. *Journal of Analytical Atomic Spectrometry* **25**, 1402–1409 (2010).
7. Strok, M., Baya, P. A. & Hintelmann, H. The mercury isotope composition of Arctic coastal seawater. *Comptes Rendus Geoscience* **347**, 368–376 (2015).
8. Jiskra, M., Sonke, J. E., Agnan, Y., Helmig, D. & Obrist, D. Insights from mercury stable isotopes on terrestrial-atmosphere exchange of Hg(0) in the Arctic tundra. *Biogeosciences* **16**, 4051–4064 (2019).
9. Jiskra, M. *et al.* Automated Stable Isotope Sampling of Gaseous Elemental Mercury (ISO-GEM): Insights into GEM Emissions from Building Surfaces. *Environmental Science & Technology* **53**, 4346–4354 (2019).

10. Heimbürger, L. E. *et al.* Shallow methylmercury production in the marginal sea ice zone of the central Arctic Ocean. *Scientific Reports* **doi:10.1038/srep10318**, (2015).
11. Wiederhold, J. G. *et al.* Equilibrium mercury isotope fractionation between dissolved Hg(II) species and thiol-bound Hg. *Environmental Science and Technology* **44**, 4191–4197 (2010).
12. Gehrke, G. E., Blum, J. D. & Meyers, P. A. The geochemical behavior and isotopic composition of Hg in a mid-Pleistocene western Mediterranean sapropel. *Geochimica et Cosmochimca Acta* **73**, 1651–1665 (2009).
13. Ogrinc, N., Hintelmann, H., Kotnik, J., Horvatl, M. & Pirrone, N. Sources of mercury in deep-sea sediments of the Mediterranean Sea as revealed by mercury stable isotopes. *Scientific Reports* **9**, 11626 (2019).
14. Bergquist, B. A. & Blum, J. D. Mass-Dependent and -Independent Fractionation of Hg Isotopes by Photoreduction in Aquatic Systems. *Science* **318**, 417–420 (2007).
15. Kritee, K., Motta, L. C., Blum, J. D., Tsui, M. T.-K. & Reinfelder, J. R. Photomicrobial Visible Light-Induced Magnetic Mass Independent Fractionation of Mercury in a Marine Microalga. *ACS Earth Space Chem.* **2**, 432–440 (2018).
16. Motta, L. C., Kritee, K., Blum, J. D., Tsz-Ki Tsui, M. & Reinfelder, J. R. Mercury Isotope Fractionation during the Photochemical Reduction of Hg(II) Coordinated with Organic Ligands. *The journal of physical chemistry. A* (2020) doi:10.1021/acs.jpca.9b06308.
17. Zheng, W. & Hintelmann, H. Isotope Fractionation of Mercury during Its Photochemical Reduction by Low-Molecular-Weight Organic Compounds. *Journal of Physical Chemistry A* **114**, 4246–4253 (2010).
18. Motta, L. C. *et al.* Mercury Cycling in the North Pacific Subtropical Gyre as Revealed by Mercury Stable Isotope Ratios. *Global Biogeochemical Cycles* **33**, 777–794 (2019).
19. Lamborg, C. H., Rolfhus, K. R., Fitzgerald, W. F. & Kim, G. The atmospheric cycling and air–sea exchange of mercury species in the South and equatorial Atlantic Ocean. *Deep Sea Research Part II: Topical Studies in Oceanography* **46**, 957–977 (1999).

20. Holmes, C. D., Jacob, D. J., Mason, R. P. & Jaffe, D. A. Sources and deposition of reactive gaseous mercury in the marine atmosphere. *Atmospheric Environment* **43**, 2278–2285 (2009).
21. MDN. Mercury Deposition Network. http://nadp.slh.wisc.edu/MDN/ (2020).
22. Sheu, G.-R. & Lin, N.-H. Characterizations of wet mercury deposition to a remote islet (Pengjiayu) in the subtropical Northwest Pacific Ocean. *Atmospheric Environment* **77**, 474–481 (2013).
23. Marumoto, K. & Matsuyama, A. Mercury speciation in wet deposition samples collected from a coastal area of Minamata Bay. *Atmospheric Environment* **86**, 220–227 (2014).
24. Fostier, A.-H. *et al.* Mercury fluxes in a natural forested Amazonian catchment (Serra do Navio, Amapá State, Brazil). *Science of The Total Environment* **260**, 201–211 (2000).
25. Tessier, E. *et al.* Mercury mobilization in soil from a rainfall event in a Tropical forest (French Guyana). *J. Phys. IV France* **107**, 1301–1304 (2003).
26. Dutt, U., Nelson, P. F., Morrison, A. L. & Strezov, V. Mercury wet deposition and coal-fired power station contributions: An Australian study. *Fuel Processing Technology* **90**, 1354–1359 (2009).
27. Sprovieri, F. *et al.* Five-year records of mercury wet deposition flux at GMOS sites in the Northern and Southern hemispheres. *ATMOSPHERIC CHEMISTRY AND PHYSICS* **17**, 2689–2708 (2017).
28. Shah, V. & Jaeglé, L. Subtropical subsidence and surface deposition of oxidized mercury produced in the free troposphere. *Atmospheric Chemistry and Physics* **17**, 8999–9017 (2017).
29. Horowitz, H. M. *et al.* A new mechanism for atmospheric mercury redox chemistry: implications for the global mercury budget. *Atmospheric Chemistry and Physics* **17**, 6353–6371 (2017).
30. Sprovieri, F. *et al.* Atmospheric mercury concentrations observed at ground-based monitoring sites globally distributed in the framework of the GMOS network. *ATMOSPHERIC CHEMISTRY AND PHYSICS* **16**, 11915–11935 (2016).
31. Andersson, M. E., Gårdfeldt, K., Wängberg, I. & Strömberg, D. Determination of Henry's law constant for elemental mercury. *Chemosphere* **73**, 587–592 (2008).

32. Nightingale, P. D. *et al.* In situ evaluation of air-sea gas exchange parameterizations using novel conservative and volatile tracers. *Global Biogeochemical Cycles* **14**, 373–387 (2000).
33. Kuss, J., Holzmann, J. & Ludwig, R. An Elemental Mercury Diffusion Coefficient for Natural Waters Determined by Molecular Dynamics Simulation. *Environ. Sci. Technol.* **43**, 3183–3186 (2009).
34. Bieser, J., Angot, H., Slemr, F. & Martin, L. Atmospheric mercury in the Southern Hemisphere – Part 2: Source apportionment analysis at Cape Point station, South Africa. *Atmospheric Chemistry and Physics Discussions* **2020**, 1–17 (2020).
35. Blum, J. D. & Johnson, M. W. Recent Developments in Mercury Stable Isotope Analysis. *Reviews in Mineralogy and Geochemistry* **82**, 733–757 (2017).
36. Zhang, Y. *et al.* A Coupled Global Atmosphere-Ocean Model for Air-Sea Exchange of Mercury: Insights into Wet Deposition and Atmospheric Redox Chemistry. *Environmental Science & Technology* **53**, 5052–5061 (2019).
37. Andersson, M. E. *et al.* Seasonal and daily variation of mercury evasion at coastal and off shore sites from the Mediterranean Sea. *Marine Chemistry* **104**, 214–226 (2007).
38. Vermeesch, P. IsoplotR: A free and open toolbox for geochronology. *Geoscience Frontiers* **9**, 1479–1493 (2018).